REPORT DOCUMENTATION PAGE

AFRL-SR-BL-TR-98-

1663

1. AGENCY USE ONLY *(Leave blank)*	2. REPORT DATE	3. REPORT TYPE AND DATES COVERED
	AUGUST 1998	FINAL REPORT 15 Mar 95 - 14 Mar 98

4. TITLE AND SUBTITLE
POLYCOMPONENT FUNCTINALLY GRADED MATERIALS FOR THERMAL BARRIER SYSTEMS

5. FUNDING NUMBERS
F49620-95-C-0028

61102F
2306/AS

6. AUTHOR(S)
MELVIN R. JACKSON

7. PERFORMING ORGANIZATION NAME(S) AND ADDRESS(ES)
GENERAL ELECTRIC CO
GE CORP RESEARCH & DEVELOPMENT
SCHENECTADY, NY 12301

8. PERFORMING ORGANIZATION REPORT NUMBER

9. SPONSORING/MONITORING AGENCY NAME(S) AND ADDRESS(ES)
AIR FORCE OFFICE OF SCIENTIFIC RESEARCH (AFOSR)
110 DUNCAN AVENUE ROOM B115
BOLLING AFB DC 20332-8050

10. SPONSORING/MONITORING AGENCY REPORT NUMBER

11. SUPPLEMENTARY NOTES

12a. DISTRIBUTION AVAILABILITY STATEMENT
APPROVED FOR PUBLIC RELEASE, DISTRIBUTION IS UNLIMITED

12b. DISTRIBUTION CODE

13. ABSTRACT *(Maximum 200 words)*

Functionally graded materials (FGMs) offer benefits for thermal barrier coating (TBC) systems for aircraft and power generation gas turbines. A preferred FGM, including the insulating ceramic outer surface and a graded inner structure on a superalloy substrate, will act both to minimize stresses due to the temperature difference between the outer surface of the FGM and the underlying substrate, and also to protect the substrate from environmental attack. Most bond coats in use are not functionally graded; they are monolithic, or, are made of discrete layers of different combinations of materials. Currently, deficiencies in bond coat performance directly impact and reduce the performance and life of TBC systems. This research is directed toward improving the durability and performance of thermal barrier systems via improved understanding of the interrelationships between the thermophysical, chemical and mechanical properties. Durability also may be improved by decreasing ceramic thickness. If nanocrystalline ceramics are shown to offer improved insulating performance, this will allow decreased ceramic thickness for performance equivalent to current ceramic layers. The overall objective of the research was to develop fundamental understandings of the physical and mechanical properties of polycomponent (three or more constituent) FGM systems as a function of phase constituents, phase volume, and microstructure. The use of three or more components in an FGM system permits the decoupling of previously dependent physical properties. For example, in a binary metal oxide-metal graded system, thermal conductivity and thermal expansion are not independent of one another, because both are functions of the volume fraction metal oxide.

14. SUBJECT TERMS	15. NUMBER OF PAGES
	78
	16. PRICE CODE

17. SECURITY CLASSIFICATION OF REPORT	18. SECURITY CLASSIFICATION OF THIS PAGE	19. SECURITY CLASSIFICATION OF ABSTRACT	20. LIMITATION OF ABSTRACT
UNCLASSIFIED	UNCLASSIFIED	UNCLASSIFIED	

Polycomponent Functionally Graded Materials for Thermal Barrier Systems

Contract No. F49620-95-C-0028

AFOSR Program Manager: Dr. Spencer Wu
AFOSR/NA
Directorate of Aerospace and Materials Sciences
110 Duncan Avenue, Room B115
Bolling AFB, DC 20332-8050

Research Contributors

Dr. M.R. Jackson, Dr. A.M. Ritter, Dr. M.F.X. Gigliotti,
Dr. J. Dobbs, Dr. J.-C. Zhao, GE-CRD, Physical Metallurgy Laboratory
Dr. A.C. Kaya, Dr. J Zuiker, Dr. J. Gallo, GE-CRD Engineering Mechanics Laboratory
Dr. Merrilea Mayo, Professor, and Dr. Srinivasan Raghavan, Post-Doctoral Researcher, Pennsylvania State University
Dr. John Lannutti, Ohio State University, Professor

Table of Contents

Abstract

Functionally graded materials (FGMs) offer benefits for thermal barrier coating (TBC) systems for aircraft and power generation gas turbines. A preferred FGM, including the insulating ceramic outer surface and a graded inner structure on a superalloy substrate, will act both to minimize stresses due to the temperature difference between the outer surface of the FGM and the underlying substrate, and also to protect the substrate from environmental attack. Most bond coats in use are not functionally graded; they are monolithic, or, are made of discrete layers of different combinations of materials. Currently, deficiencies in bond coat performance directly impact and reduce the performance and life of TBC systems. This research is directed toward improving the durability and performance of thermal barrier systems via improved understanding of the interrelationships between the thermophysical, chemical and mechanical properties. Durability also may be improved by decreasing ceramic thickness. If nanocrystalline ceramics could be shown to offer improved insulating performance, decreased ceramic thickness would be possiblefor performance equivalent to current ceramic layers.
The overall objective of the research was to develop fundamental understanding of the physical and mechanical properties of polycomponent (three or more constituent) FGM systems as a function of phase constituents, phase volume, and microstructure. The use of three or more components in an FGM system permits the decoupling of previously dependent physical properties. For example, in a binary metal oxide-metal graded system, thermal conductivity and thermal expansion are not independent of one another, because both are functions of the volume fraction metal oxide. In contrast, the concept of polycomponent systems of this study allows selection of one phase constituent for thermal expansion coefficient, a second for environmental resistance, and a third for elastic modulus, and so forth, with only the outer ceramic layer having non-metallic thermal conductivity. The phase constituents must be selected for mutual thermodynamic stability because of the high service temperatures.

1.0 Executive Summary

In jet engines, thermal barrier coatings (TBCs) are used to extend component life beyond expected design life. If adherence of the TBC can be maintained reliably, the insulating behavior of the ceramic layer can be factored fully into the design, which will greatly increase engine performance. Use of functionally graded materials (FGMs) to provide thermal expansion gradients from the metal substrate to the outer, low-expansion ceramic FGM layer may achieve the required adherence and reliability. However, graded structures that rely on ceramic phases to provide the decreased expansion produce the undesirable effects of increasing the temperature in the outermost metallic regions of the FGM, and reducing significantly the strain tolerance of the bond coat-TBC FGM system over a broad temperature range. Higher temperatures lead to more rapid oxidative attack of the metallic phase, which can increase the possibility of spallation of the outer ceramic layer. Poorer strain tolerance may lead to cracking and delamination, where a more ductile, all-metal system may deform locally rather than fracture.

The program was undertaken to enhance the present understanding and state of the art for both high-temperature FGMs and thermal barrier systems. We have characterized the response of mechanical, physical, and chemical behavior that develops in polycomponent (>/=3 phases) FGM systems, incorporating low-expansion/high-thermal-conductivity phases between substrate and insulating outer layers (Figure 1-1), and have formulated models that predict the FGM stresses and temperatures. Nanocrystalline ceramic layers have been evaluated to explore the possibility of reduced thermal conductivity benefits.

- Systems of graded material combinations have been identified which have interfacial expansion behavior equivalent to the outer ceramic layer expansion, while still relying on phases with high thermal conductivity.
- Such graded material combinations are fabricable by one-step deposition processing.
- The nanoceramic structures offer a wide variety of controlled microstructures (grain size, porosity), and therefore, controlled thermal conductivity, but no reduction in conductivity related to feature size is apparent.

2.0 Program Objectives

The study of polycomponent FGM systems has sought to achieve greater independence in selecting mechanical, physical, and chemical behavior in high-temperature systems.

The objective of the research was to characterize and understand the interrelationships in behavior that develop in polycomponent, functionally graded material (FGM) systems suited to thermal protection of underlying superalloy components from hot gases at 1350-1650 C. The focus was on the incorporation of three or more materials in the FGM to increase the ability to control mechanical, physical, and chemical behavior independently. Concurrent and interrelated sub-objectives included

- Stability of FGM microstructures and properties in thermal environments (thermodynamic, morphological, mechanical, environmental stabilities)
- Prediction of behavior of polycomponent systems (generation and validation of physical/mathematical models)
- Influence of nanophase structures on thermal behavior (interaction of thermal energy with FGM nanostructures)

The program concentrated on structures appropriately sized for real turbine hardware (entire FGM 250-400 μm) containing phases that address the required physical, mechanical and thermal behavior.

3.0 Technical Background

Major improvements in turbine efficiency and performance are achievable if the thermal barrier system can be relied upon to survive throughout the design life. Polycomponent functionally graded materials may be a route to such a thermal barrier system.

3.1 Introduction

In modern jet engines and gas turbines, hot-section gas path surfaces are exposed to oxidizing gases at temperatures exceeding 1350 C, and reaching as high as 1650 C. These temperatures require an enormous cooling air capacity to prevent melting or severe environmental attack and structural weakening of the metal structures. This huge cooling air burden has a negative impact on system performance and efficiency. In addition, for

some components, geometric and manufacturing limits may prevent effective cooling of a portion of the outer surfaces.

For a number of years, stationary structures such as the combustor, transition pieces, and side wall bands of the turbine nozzles have been thermally protected by a thin layer of ceramic, which is generally deposited by plasma deposition. Zirconia, modified by yttria to reduce phase transformation stresses, has been found to be most successful at providing thermal protection because it has very low thermal conductivity and because it remains adherent to the substrate better than most other ceramics. With thermal conductivity reduced to about 1/20 that of the metal substrate, zirconia provides a drop in maximum metal temperature of between 25 and 100 C, depending on ceramic thickness and aggressiveness of substrate cooling.

As will be discussed, rough surfaces of plasma-sprayed MCrAlY compositions are often used between the substrate and the thermal barrier coating (TBC). These MCrAlY layers provide environmental resistance to the substrate when the ceramic spalls from the surface, exposing the metal structure to the hot gases. They also serve as a bond coating by providing a convoluted surface for mechanical interlocking with the TBC. Although the thermal expansion difference for zirconia and Ni superalloys is small relative to other ceramics, it is still large enough to create tremendous stresses, leading to early TBC loss. Considerable effort has gone into microstructural control of the TBC and the TBC/bond coat interface to minimize the expansion-driven stresses.

Thermal barrier coatings are now finding wider use in airfoil surfaces of stationary nozzles and rotating turbine blades or buckets. Aerodynamic limits on design-allowable TBC coating thickness have required the consideration of other deposition methods, such as electron beam evaporation of the ceramic, to provide a thin, smooth-surfaced coating.

To the present, the thermal barrier systems have been used to extend component life beyond the design life by providing insulation, to reduce average metal temperatures and reduce local thermal spikes. However, reliability of the TBC adherence has been insufficient to allow the TBC to be incorporated into the design.

Major improvements in turbine efficiency and performance are achievable if the TBC can be relied upon to survive throughout the design life. These improvements result directly

from allowing higher gas temperatures without a rise in metal temperatures, or allowing a reduction in cooling air burden without a rise in metal temperatures, or a combination of reduced cooling air and higher flame temperatures.

Functionally graded materials have been considered as bond coatings in thermal barrier systems. They offer the possibility of bond enhancement by providing a gradient in thermal expansion between the Ni superalloy and the ceramic TBC. FGMs have been suggested as structural materials, capable of carrying load or performing other functions most effectively, by tailoring the material properties through the thickness of the FGM to exactly match the performance needs of the structure. The FGMs can be made of a number of homogeneous-composition layers, or the components of the FGM can be graded continuously through the thickness.

For surface coatings applied for wear resistance, thermal resistance, etc., the use of FGMs as bond enhancement structures offers improved performance wherever surface coatings are subject to spallation or delamination. In the design of FGM characteristics, the surface coating can be considered as part of the FGM system for achieving desired performance. Spallation and delamination failures are frequently driven by thermal expansion differences between the surface coating and the substrate, as in the thermal barrier system.

Needed Improvements to FGMs: In earlier attempts at employing FGMs in the bond coat function, metals such as MCrAlY compositions have been graded with ceramics such as zirconia or alumina. This properly addresses the problems of a discontinuous step in expansion behavior at the metal bond coat/TBC interface (Figure 3-1). However, this does not fully address system requirements. By effectively decreasing the thermal conductivity of the bond coat by the addition of ceramic, the temperature reached by the outermost metal phase of the FGM is increased beyond temperatures reached in all-metallic bond coatings (Figure 3-2). These higher metal temperatures can lead to more rapid oxidation of the metal component of the FGM, with the growth stresses leading to premature failure of the thermal barrier system. For many superalloys, oxidation rates at temperatures above approximately 1000 C increase by a factor of 50% or more for each 10 C increase in surface temperature.

Models of FGMs could be used to predict such increases in metal phase temperature. Several simple models of FGM structures have been developed. These have been used to predict stress and temperature through the FGM structure, but in general these models have dealt with large structural FGMs rather than FGMs with thicknesses on the order of 250-400 μm, is required for gas turbine applications. Rigorous analyses are needed to address property estimation, heat transfer, stress, and temperature of the system. Nanocrystalline zirconia ceramics, which have been developed only in the last 8-10 years, may provide a new technological approach to TBCs, and, by extension, to FGMs. Nanocrystalline ceramics can plastically deform under stress at lower temperatures than can coarse-grained ceramics [1,2]. Some plastic deformation may be beneficial to TBCs, since it can allow relaxation of thermal mismatch stresses and can help prevent thermal mismatch cracking and spallation. In addition, there has been speculation that nanocrystalline TBCs will have lower thermal conductivity than conventional TBCs because of their ultrafine grain and pore sizes (see Section 4.4). Lower thermal conductivities would allow thinner coatings to be used, thereby solving several additional problems related to TBCs: reducing the load of the TBC on turbine blades, allowing TBCs to be incorporated into turbine design even when clearances on the turbine throat area dimensions are tight, and decreasing the available flaw population in the TBC (i.e., decreasing the number of potential crack initiation sites, which increases with increasing volume of material according to Weibull statistics). For these reasons it seems advantageous to consider incorporating nanocrystalline ceramics into the next evolutionary step in thermal barrier systems: replacing the conventional bond coat and coarse-grained zirconia TBC with the more integrated and environmentally more rugged FGM (graded metal bond coat with nanoceramic TBC).

3.2 Thermal Barrier Systems - Bond Coatings and Ceramics

Thermal barrier coating systems - consisting of an insulating ceramic layer, or topcoat, an oxidation-resistant bond coat, and a metallic substrate - have been under development for the last 20 years. They are designed to reduce heat transfer to metal components, allowing either use of higher turbine inlet temperatures or reduced cooling air. Use of these coatings has been somewhat limited by reliability issues, primarily spallation of the ceramic

topcoat [3]. Because of this, considerable research has been devoted to understanding the mechanisms of TBC failure, and the influence of processing variables on TBC microstructure and cyclic life.

The coatings are generally fabricated by deposition of a metallic bond coat onto the part, followed by deposition of a ceramic insulating layer onto the bond coat [4]. Deposition is commonly done by either thermal spraying - e.g., air plasma-spraying (APS) or low-pressure plasma deposition (LPPD) - or by physical vapor deposition (PVD) [4].

The ceramic topcoat that has been most commonly used is ZrO2, which has a very low thermal conductivity and a thermal expansion coefficient reasonably close to that of superalloys. In its binary form ZrO2 undergoes a crystallographic transformation from tetragonal to monoclinic, accompanied by a large volume change, during cooling from service temperatures [5,6]. Since the volume change can cause cracking and spallation of the coating, additions such as Y2O3, CaO, CeO2,Yb2O3, or MgO have been studied [7-10] to partially or fully eliminate the phase transformation. Studies on yttria-stabilized ZrO2 have found [11] that the optimum composition range for resisting thermal cycling damage is 6-8 wt% yttria, which results in partial stabilization of the ZrO2 (PSZ) [5]. The effect of other additions, like CeO2, to the resistance of ZrO2-based coatings to thermal shock has also been evaluated [9,12].

Processing research on the ceramic topcoat has been focused on general material properties, such as modulus, coefficient of thermal conductivity (CTE), thermal conductivity, and strength [13], and on the effect of various microstructures on the durability of the ceramic during thermal cycling. It has been found, for example, that cyclic life was enhanced for PVD coatings with a columnar microstructure, relative to a dense plasma-sprayed structure [14]. Similarly, better thermal shock resistance and thermal insulation have been reported [8] for plasma-sprayed coatings with vertical microcracks. Both of these effects are related to the compliance of the coating, as discussed below.

The bond coat is usually of an MCrAlY composition (where 'M' is Ni, Co, or both) and is more oxidation-resistant and corrosion-resistant than the underlying superalloy part. Since bond coat oxidation is a major factor in TBC failure, work on bond coats has dealt with the effects of oxidation rate on TBC life, as discussed below, and with alloying additions

that may increase oxidation resistance, such as Yb [15] and Hf and Si [16]. Oxidation resistance has also been substantially improved by aluminiding the bond coat prior to deposition of the ceramic topcoat [3]. This process, usually done by pack aluminiding, results in an increased Al content on the outer surface of the bond coat. The effect of increased bond coat strength on TBC life has also been investigated [3]. It was found that solute strengtheners, grain boundary strengtheners, and elements to increase γ' content added to MCrAlY-based compositions resulted in improved cyclic lives, especially when the coatings were overaluminided. Bond coat roughness also has been found to be a factor in TBC life: better topcoat adhesion is commonly observed with increased bond coat roughness [3,16] for plasma-sprayed TBCs as a result of mechanical interlocking.

TBC failure often occurs by cracking and spallation of the ceramic topcoat. Mechanisms for this failure include [3] spallation caused by thermal stresses arising during cooling of the TBC; sintering of the ceramic, which produces reduced resistance to thermal shock; microcracking of the topcoat; bond coat oxidation, which strains the ceramic topcoat; and creep of the bond coat or substrate. The microstructure, properties and failure of conventional TBCs have been studied in some detail [3,17,18]. At shorter lifetimes, cracks are generally found in the ceramic near the bond coat/ceramic interface, with the cracks running parallel to that interface [3]. The cracks appear to have been generated during cooling by the stresses arising from the thermal expansion mismatch between bond coat and ceramic. Reduction of these stresses in the TBC by altering the processing conditions [19] or by better matching the CTE of topcoat and bond coat [20] has been investigated as a route to increase TBC durability. Accommodation of cyclic thermal stresses may be increased by producing a segmented ceramic topcoat structure by grooving the substrate surface prior to plasma-spraying the coating [18].

Techniques such as increasing the compliance of the ceramic layer by entrained porosity and vertical microcracking have been tried as a means to increase TBC life. Increased porosity in the topcoat was shown to increase TBC life [18], although this benefit may disappear after long service lives because of sintering of the ceramic. Processing of the topcoat to produce a vertically cracked compliant structure is effective [8], but the presence of the cracks may allow infiltration of the ceramic by corrosive liquids [8] or

other impurities [21]. TBC system compliance also can be increased by using a compliant layer such as Feltmetal pads between the topcoat and bond coat or by using a porous plasma-sprayed metallic layer as the bond coat [18].

Stresses also may be reduced by producing a composite or a graded FGM structure [18]. Increased coating adhesion and TBC lives have been shown for microlaminated structures produced by plasma deposition [22,23]. Eaton and Novak [24] investigated the response of graded CoCrAlY/ceramic structures to thermal cycling. The thermal shock resistance of graded structures was found to be superior to that of monolithic coatings for bond coats consisting of mixtures of NiCrAlY and ZrO2 stabilized by MgO or Y2O3 [25].

TBC failure from bond coat oxidation has been observed for bond coats processed by plasma-spraying [3,26] and by PVD [27]. For both monolithic and MCrAlY/ZrO2 . Y2O3 composite bond coats, alumina layers were observed to form between the metal and ZrO2 . Y2O3 [17,26,28,29], with other oxides such as Cr2O3 [29] NiO [26] and spinel [17,28] forming after the Al in the MCrAlY was sufficiently depleted. The presence of these growing oxide layers can contribute to coating failure by reducing the overall ductility of the bond coat and the bond coat/substrate interface [30] and by straining the adjacent ZrO2 . Y2O3 layer [17,29].

Despite the amount of research that has been carried out for TBC processing and failure mechanisms, reliability is not at a level where the TBC performance can be guaranteed for airfoil design. The concept of using FGMs to increase that reliability may be important to achieving the full potential of TBCs.

3.3 Functionally Graded Materials.

Functionally graded materials (FGMs) are objects whose composition and structure vary with position, and have been selected to yield preferred performance in response to position-dependent requirements. Thermal barrier coatings - an outer insulating ceramic, a bond coat, and an underlying substrate - can be viewed as coarsely stepped functionally graded materials.

An early description of the TBC systems, comprising (1) zirconia or partially stabilized zirconia outer layer; (2) a NiCrAlY type bond coat; and (3) a superalloy substrate was provided by Leibert and Stecura in 1977 [31]. This approach had been anticipated by

Dowell, who described multi-layer coating of internal combustion chambers - where an inner layer was a nickel-aluminum alloy, a second layer was the nickel aluminum alloy with zirconium oxide, and an outer layer is primarily zirconium oxide [32]. Considerable work (summarized in Section 3.2) has been directed at monolithic bond coat compositions to improve oxidation resistance, mechanical compliance, and ceramic adhesion. A continuous spatial variation of bond coat composition and properties was proposed by Goward, Grey, and Krutenat, who described a continuously graded zirconia-NiCoCrAlY bond coat [33].

A large impetus to development of functionally graded materials was provided by the Science and Technology Agency of the Government of Japan, who carried out a 5-year project between 1987 and 1992 to develop the materials and process technology for heat resistant FGMs in thermal gradients. A major focus of this effort was on thermal barrier systems [34]. The project resulted in several viable processing techniques for graded superalloy-ceramic structures [35].

Graded binary superalloy-ceramic structures have demonstrated mechanical performance improvements as bond coats for thermal barrier systems. The residual thermal stresses present in parts as a result of fabrication can be reduced by grading the structure [36]. Laser thermal shock tests coupled with acoustic emission showed that ZrO2-based thermal barrier systems were more resistant to thermal shock when the structure was graded to NiCrAlY, rather than achieved in a single step [37]. Use of a graded cermet structure within the bond coat was reported to give preferred performance in a thermal barrier coating system applied to a diesel engine [38].

Chemical grading of the bond coat has improved TBC system performance where TBC failure is caused by oxidation of the bond coat and spallation of the TBC. A hypothesis is that oxygen diffusing atomically in the partially stabilized zirconia outer layer, or migrating as a gas in cracks, can attack the bond coat, forming mixed oxides that cause the outer TBC layer to spall. Typically, after deposition of the bond coat and prior to deposition of the zirconia, an aluminizing treatment is applied to the bond coat, creating an aluminum gradient and improving its surface stability. TBCs on Mar M247 had longer lives for the case of pre-aluminized bond coats [39].

Clearly, there has been improvement in mechanical performance at the bond coat/TBC interface through the use of FGMs. However, incorporating low-conductivity ceramics in the graded region has led to increased temperatures in the local metallic-ceramic region closest to the ceramic thermal barrier layer. Since TBC failure is related to oxidation of the bond coat in conventional TBCs, it is not surprising that FGMs with ceramic gradients have suffered from the same limitations. Reliability must still be improved substantially.

3.4 Modeling the Behavior of FGM Composites

The relatively low elastic modulus and small thickness of ceramic TBCs, compared with the metal substrate, results in the TBC contributing little to overall component stiffness. The coating is thus generally in a strain-controlled environment and the coating stress is proportional to its elastic modulus. Because of the relatively high mismatch of thermal expansion coefficients, applying homogeneous ceramic coatings onto metal substrates creates very high residual and thermal stresses. As a result, early cracking and delamination may break the thermal insulation and considerably shorten the life of the component.

For plasma-sprayed coatings, the delamination of the ceramic top coat from the bond coat is due to progressive crack growth, leading to a final catastrophic spalling event. Oxidation of the bond coat to form Al2O3 at the interface with the TBC provides a crack path. In EB-PVD coatings the cracking process is sudden rather than progressive through the Al2O3 layer [40].

In general, three common modes of delamination failure have been observed in TBC systems: free-edge delamination, buckling failure far from free edges, and delamination from transverse cracks (Figure 3-3).

In conventional TBCs, where each layer (substrate, bond coat, and TBC) is homogeneous, the properties through the thickness are piecewise constant and therefore they exhibit sharp discontinuities between layers. Stress analyses at the edges of such interfaces (case 1 in Figure 3-3) show that the normal and the shearing stress components perpendicular to the interface are very high. In fact, elastic analyses predict stress singularities near free edges.

In FGM structures where the volume fractions of metal and ceramic vary continuously in the thickness direction, the nonhomogeneous medium will exhibit the desired thermomechanical properties [41-43]. The smooth variation of properties reduces the residual and thermal stresses, and the bond strength along the coating/substrate interface is increased.

In multilayered FGMs, where the composite medium consists of multiple dissimilar homogeneous layers (with discontinuous thermal and mechanical properties), varying in successive layers from metal to ceramic, the FGM properties such as thermal expansion coefficient and modulus change gradually from the substrate to the FGM surface. Applications of this type of graded coating can be found in diesel engine TBCs [40] (Figure 3-4).

In the multilayered FGM system where each layer is homogeneous, the stress-free ends contain singular points where the interfaces of bonded dissimilar materials intersect the free surface. However, in the continuous FGM coatings [44-46], the free-edge stress concentrations will be much lower than in multilayered homogeneous coatings. If the discontinuity in material property distribution can be eliminated, then stresses will be bounded.

For fracture mechanics of cracks near interfaces, continuously varying FGMs avoid two other anomalies that complicate the analysis of sharp interfaces:

- Oscillatory stress and displacement fields near the interface crack-tip [46].
- Non-square-root power singularity for a crack approaching and terminating at the interface [47].

Despite the amount of modeling performed for FGMs, Miller, Lannutti, and Yancey [48] found mathematical guidelines available in the literature were difficult to use for the design of FGMs, previous designs having been based on either intuition or trial-and-error. A clear need for some form of numerical guidance was emphasized. Subsequently, Lannutti's analysis of the effects of different materials combinations on residual compressive stresses and curvature [49] showed little importance of ceramic thermal conductivity on thermal shock resistance in properly designed FGMs.

Miller, Lannutti and Noebe developed a model for the design of FGMs based on the minimization of strain energy [50, 55]. This model made accurate predictions of sample curvature and the visual results of excessive internal compressive stress. The model also made estimates of the effects of thermal stress on internal residual stresses as a function of exposure time and temperature. These results were validated using a thermal cycling rig.

Itoh and Kashiwaya analyzed the residual stresses of FGMs induced during the fabrication process by comparing several graded systems [36]. The effects of gradation size and material constants, such as Young's modulus and thermal expansion coefficients, on the residual stress of the FGM structure were investigated.

In detailed finite element stress analyses of FGM continuous and multilayer TBCs bonded to metal substrates [51], the continuous coating (a graded particulate composite of Rene 41 and zirconia) was compared with multilayer coatings of one, two or four homogeneous layers with stepwise changing volume fractions. Considerable reduction of free-edge stresses was accomplished using the continuous coating. The sharp interfaces and discontinuous thermomechanical properties in multilayer coatings required consideration of free-edge stress singularities and oscillatory stress fields near interface crack tips.

In a finite element solution of multilayer coatings subjected to thermal stresses [52], the power of stress singularity at the free-edges was calculated analytically, and the stress intensity factors were determined by curve fitting to the finite element stress results. A similar approach was used for continuous FGM coatings [45]. Analytical solutions exist for edge-cracked FGM plates [53] and for an interface crack in a FGM coated homogeneous substrate [46].

An analysis of the fracture problem of debonding of FGM thermal barrier coatings from metal substrates [46] considered various coating thicknesses and different functional forms of the property gradation through the coating thickness. More recently, elastoplastic analysis of multilayered materials and FGM interfaces for cyclic thermal loading [54] considered effects of metallic layer plasticity.

The sophistication of modeling of FGMs has increased over the past several years. Simple models are available to aid in thermal system definition, and finite element models exist that can treat the FGM thermal barrier system with greater rigor. These models need to be

exercised to aid in developing a fundamental understanding of these materials, and in increasing their utility.

3.5 Nanocrystalline Ceramics and Thermal Conductivity

For a material to be an effective thermal barrier coating, it must have a low thermal conductivity; equivalently, it must prevent the transmission of heat by phonons. Phonons are the elastic energy waves generated by lattice vibrations; their mean free path sets the thermal conductivity, according to

$$K = v_0 \, Cv \, \lambda / 3 \qquad (3.5\text{-}1)$$

where K is the thermal conductivity, v_0 is the phonon velocity, Cv is the heat capacity of the solid (essentially a constant above room temperature), and λ is the phonon mean free path [61].

The mean free path of phonons would be infinite, leading to an infinite thermal conductivity and perfect heat transmission, were it not for phonon-phonon scattering events. Because of phonon-phonon interactions, λ is reduced to a few nanometers at low temperatures (0 C) [62] and a few angstroms at higher temperatures (e.g., 1000 C) [63], where the mean free path between interactions is even shorter. For a given temperature and material, however, the mean free path length - and consequently, the thermal conductivity - can be considered as having an intrinsically finite, constant value. Generally one does not consider microstructure when invoking equation 3.5-1. Theoretically, however, certain microstructural features, such as grain and pore boundaries, also can scatter phonons and reduce λ. It has long been recognized that if sufficiently small grain sizes could be produced, the distance between grain boundaries (which act as scattering centers) would approach the phonon mean free path length. In that case, grain boundary scattering would be a significant addition to the existing phonon-phonon scattering, and materials could be produced with markedly reduced thermal conductivity [64]. For substantial scattering by grain boundaries (in addition to that by phonons), the mean free path would become [64,65]

$$\lambda = 1/[(\lambda_{\text{boundary}})^{-1} + (\lambda_{\text{phonon}})^{-1}] \qquad (3.5\text{-}2)$$

and the thermal conductivity would then be

$$K = v_0 Cv / (3 [(\lambda_{boundary})^{-1} + (\lambda_{phonon})^{-1}]) \quad (3.5\text{-}3)$$

Large reductions in thermal conductivity have been experimentally observed for a few ultrafine-grained materials - in particular, selenium and carbon crystallized from the amorphous state [64]. However, a published account of this effect in more traditional refractory materials, such as oxide ceramics, has yet to appear. The reason is largely that most oxide ceramics are made by the compaction and sintering of particles, and the grain sizes that result from this technique - typically 0.5 to 10 μm - are much too large to cause any significant scattering effects.

Yttria-partially stabilized zirconia (ZrO2-3 mol%Y2O3) is often used as a thermal barrier coating because of its low thermal conductivity (very effective phonon-phonon scattering). Very recently, it has become possible to produce ZrO2-3 mol%Y2O3 with grain sizes 10 to 100 times smaller than conventional ZrO2-3 mol%Y2O3 [66-68], just at the point where an effect of grain size on the mean phonon path length should be seen. Although it may be possible to fabricate thermal barrier coatings with lower thermal conductivities than those used at present, the thermal conductivity of nanocrystalline ZrO2-3 mol%Y2O3 has never been reported.

The potential effect of nanocrystalline grain sizes on thermal conductivity is all the more intriguing because there is speculation [69, 70] that the grain boundaries in such materials have different structures than even conventional grain boundaries, and therefore can be thought of as a separate 'phase,' quite distinct from the lattice. In this case, the net thermal conductivity would be set by both the conductivity of the grain boundaries (of which there are more than $10^{16}/cm^3$, even for a 30-nm grain size material) and the conductivity of the lattice, in accordance with two-phase models such as those of Charvat and Kingery [71] or Litovsky [72]. Presumably, the conductivity of the grain boundaries would be significantly lower than that of the lattice, and so the net conductivity of the nanocrystalline solid would be further decreased from that of a large-grained material.

Porous (85-98% dense) nanocrystalline ZrO2-3 mol%Y2O3 can also be manufactured and is a better candidate for a thermal insulator than dense ZrO2-3 mol%Y2O3. The pores in partially sintered nanocrystalline ZrO2-3 mol%Y2O3 are even smaller than the grains, ranging from 5 nm to less than 1 nm in size; furthermore, the pores often can be tailored to

a specific size within this range [73]. The boundaries surrounding these small pores can be expected to contribute to scattering in the same manner as grain boundaries. In addition, the low thermal conductivity of the pore itself (approximately that of air) would further reduce the net conductivity.

In the most extreme case, then, as many as four factors may contribute to reduced thermal conductivity in nanocrystalline ZrO2-3 mol%Y2O3:

- Scattering of lattice phonons by grain boundaries
- Scattering of lattice phonons by pore boundaries
- Reduced thermal conductivity along the grain boundary 'phase' (caused by either a difference in heat capacity or phonon scattering ability with respect to the lattice)
- Reduced thermal conductivity associated with the pore phase (estimated as the conductivity of the gas inside the pore).

It remains to be seen which of these mechanisms dominates, and to what extent the thermal conductivity of nanocrystalline ZrO2-3 mol%Y2O3 differs from the more conventional, large-grained material counterparts. Stability of the nanocrystalline microstructural features during long thermal exposure is required to retain any added contributions of these mechanisms to thermal conductivity reduction.

4.0 Technical Approach

Understanding FGM systems with greater independence in mechanical, physical and chemical behavior is necessary to improve the reliability of high-temperature systems.

4.1 Introduction

Improved thermal barrier system reliability must be achieved for TBC thermal performance to be an important factor in turbine airfoil design. Incorporation of functionally graded materials in the thermal barrier system offers the greatest potential of reaching the necessary reliability. However, the FGMs previously considered have concentrated on creating a gradient in thermal expansion behavior without controlling the thermal conductivity of the FGM between the substrate and the ceramic outer layer of the FGM. A fundamental understanding is needed of the interrelationships in mechanical,

physical, and chemical behavior that develop in polycomponent FGM systems. Our approach to gaining this understanding has involved three major thrusts:

- Materials selection and evaluation for the individual FGM component layers
- Fabrication of the metallic portions of graded polycomponent FGMs
- Heat transfer and stress analysis and modeling
- Properties of nanocrystalline ceramic thermal barrier systems for FGMs

Improvements in thermal barrier system reliability must be achieved in thin FGMs: allowable system thickness is restricted by the aerodynamics of the airfoil design. Our approach has concentrated on evaluations of thin-section FGMs sized to be consistent with real hardware dimensions.

4.2 Polycomponent FGMs

Our approach was to select materials combinations for FGM systems after considering a number of potential candidates, and to use simple models to develop an understanding of expected system behavior. Homogeneous structures were produced and characterized, and the properties measured for more detailed modeling (see Section 4.3). FGM structures were produced without a ceramic layer. Fabrication of the metal portions of candidate FGMs was accomplished using electron beam physical vapor deposition from fixed-volume sources to build continuously graded compositions. These materials can easily be coupled to a conventional EBPVD TBC, or methods can be developed to couple to a nanocrystalline ceramic (see Section 4.4) to create the full FGM.

Materials

Several physical properties need to be varied locally within the FGM for optimal performance. The study of the ceramic portion of the FGM (see Section 4.4) considered nanocrystalline ZrO2Y2O3 to determine if enhanced thermal resistance and nanostructural stability could be achieved. The properties needed for the metal-containing portions include good oxidation resistance, metal-like thermal conductivity, graded thermal expansion, chemical compatibility with the outer TBC layer of the FGM, and chemical compatibility with the superalloy substrate. The use of a two-component graded structure, such as an oxide and an MCrAlY, cannot always provide optimal performance. The all-metallic graded structure potentially achieves much greater strain tolerance capability than

does a metal-ceramic system. This metallic graded bond coat/ceramic TBC structure avoids an expansion discontinuity and provides tolerance to macro-strains generated by the higher expansion rate behavior of the underlying superalloy substrate.

For example, consider a monolithic metallic bond coat (see Figure 3-1). The thermal conductivity and thermal expansion of the substrate and the bond coat are similar, and much greater than that of the outer ceramic layer. This results in a high thermal gradient and large length change across the ceramic, with an expansion discontinuity at the bond coat-outer layer interface.

If the bond coat is modified to become an FGM cermet, mixing ceramic and metallic phases in one or more layers, the results summarized in Figure 3-2 obtain. The metal-containing portion of the FGM now has a lower thermal conductivity than the metal matrix would have if free of ceramic, and its temperature is increased relative to the all-metallic case, with a greater risk of metallic phase oxidation and delamination of the outer TBC layer. This has been a major difficulty in the application of FGMs as TBC systems. Superalloy oxidation rates may be 50% or more greater for each 10C rise in temperature at 1000C and above. The generation of spallation stresses is faster with a more rapidly growing thermal oxide.

A metal-to-ceramic FGM is required where the thermal expansion coefficient of the metal-containing portion lies between that of the substrate and the outer TBC layer, and the thermal conductivity of the metal-containing portion is similar to the superalloy substrate (Figures 4-1 and 4-2). This can be achieved by a metal-containing portion that contains three or more constituents. Thermal conductivity and thermal expansion coefficients are plotted as functions of temperature for various material classes (Figure 4-3) [74]. The oxides have low conductivity and low thermal expansion; superalloys and aluminides have high conductivity and high expansion; while refractory metals and metal carbides have high conductivity but low thermal expansion. The refractory metals and metal carbides, then, provide a third component (after the aluminide and superalloy-like components) that can permit independent variation of thermal conductivity and thermal expansion. The elements Cr, Mo, and W each have excellent thermal conductivity (increasing from Cr to Mo to W) and expansion behavior at lower rates than the superalloys (decreasing from Cr

to Mo to W). These elements must be considered for incorporation into the metallic regime of the FGM only after a careful evaluation of their influence on environmental resistance. Although Cr yields less latitude in terms of altering FGM conductivity and expansion, it by far has a less damaging effect on superalloy environmental resistance than do W or Mo. Other components that could be considered for the metallic regime of the FGM include intermetallic phases and intermediate compounds. The phase Cr3Si is one such material that is expected to have good chemical compatibility with NiAl, and to provide reasonable oxidation resistance and thermal conductivity, in conjunction with NiAl, while still allowing graded thermal expansion behavior.

The use of three or more such components within the metal-containing portion - superalloy, NiAl, metal carbide, refractory metal, and metal intermetallic - can independently control thermal expansion and thermal conductivity to optimize the stress distribution and temperature profile through the coating. Additionally, appropriate composition modulation can maintain phase equilibria at the superalloy/FGM interface and simultaneous good oxidation resistance at the outer graded regions adjacent to the fully ceramic FGM surface layer.

A ternary diagram of the Cr-Zr-O system (Figure 4-4) [75] suggests another promising model system. With two-phase equilibria among Cr, ZrO2, and Cr2O3, a three-phase equilibrium also exists among the three phases. Because Al2O3 and Cr2O3 form an extensive series of solid solutions, (Cr,Al)2O3 solutions can likely be found in equilibrium with Cr and ZrO2. Additionally, for the Cr-Zr-C system, a two-phase equilibrium exists between Cr and ZrC, suggesting that tie lines for reactions between the chromium carbides and ZrO2 will lie in the tetrahedron defined by Cr, Cr3C2, ZrC, and ZrO2. Phases ZrO2, Al2O3, Cr3C2, Cr, and NiCrAl could constitute an initial model system.

Since NiAl and PtAl are capable of being in equilibrium with Cr and with superalloy phases, an expanded model system could include these components, particularly for the high thermal conductivity ofNiAl.

Fabrication

The sedimentation approach has been used successfully to produce graded composite structures of NiAl-Al2O3, which were evaluated by bend testing and thermal cycling [49].

In this method, powders were dispersed in a hydrophobic solvent, and the gradient in structure was developed from separately produced layers. After sedimentation, the samples were hot pressed into coupons. It would be difficult using this method to create the desired steep chemical gradients consistent with aerodynamic restrictions to added thickness.

Thermal barrier coatings are commonly fabricated using plasma-spraying and physical vapor deposition (PVD), including electron-beam PVD (EBPVD). We have considerable experience in composite and FGM structures manufactured by LPPS (low-pressure plasma spray) [29, 76-79]. Other methods which can be used to produce either coatings or coupons for testing include HIP of blended powders, sedimentation, and co-precipitation. In the plasma-spray process, powder is fed into a high-temperature plasma, and the powder particles melt in the plasma before impacting on the substrate. This process can be done by LPPS or in air (air plasma-spray, or APS). The advantage of LPPS over APS is that the LPPS coatings tend to have better bond strength and oxidation resistance [80]. These processes can easily be used to produce monolithic coatings [3] and micro-laminate, or graded, coatings [22,29]. The microstructure of the coatings is closely controlled by spray parameters.

Alternatively, PVD and EBPVD are effective methods for coating deposition. The bond coat can be deposited by PVD or by some other method, such as APS [3]. The ceramic topcoat is produced by vaporizing Y2O3-stabilized ZrO2 feedstock using a high energy electron beam [80]. This process has been used to produce smooth coatings with vertical microcracks or with columnated structures. We have developed capability of EB evaporation alternately from two separate pools (56), and we have been able to apply that deposition technology to FGMs. However, commercial sources who can produce EBPVD structures as airfoil coatings often have limited process capability beyond single-pool evaporation. Researchers at ICEBT-Kiev (57) have developed a process for deposition of a graded chemistry from single pool (described in 5.2). We have used their approach to produce graded-chemistry deposits of the appropriate materials for the metallic regime of our FGMs. The ceramic portion of such FGMs could be nanocrystalline materials produced separately and joined to the remainder of the FGM, or could be conventionally

produced EBPVD TBCs. With our fundamental studies helping to define FGM materials with substantially improved reliability, research will be required subsequently to provide technology development for practical FGM manufacture, particularly if nanoceramic technology is desired for thermal conductivity or stability/plasticity considerations.

Evaluation

We have concentrated on evaluation of homogeneous structures representative of particular locations in the FGM (both for the metallic bond coat regime and the nanoceramic TBC regime) for characterization of as-fabricated microstructures, long-time phase stability, oxidation resistance, and physical properties such as elastic modulus, thermal conductivity and thermal expansion. Microstructural characterization of as-fabricated and thermally exposed samples was done using optical microscopy, scanning electron microscopy, and electron microprobe analysis to look at phase interactions. Evaluations of the graded metallic portions of the FGM which we produced by EBPVD consisted of chemical microprobe measurements after deposition and after subsequent heat treatments.

4.3 Modeling - Heat Transfer, Stress, and Temperature Analysis

In this portion of our research, we used existing models to select materials systems and structures and to predict performance of the FGMs. One of the goals was to control independently the temperature profile (by controlling thermal conductivity), and stress distribution (by controlling thermal expansion). Simple models were used based on rule of mixtures to aid in the process of choosing the components of the FGMs and the microstructures to be evaluated for those components (see Section 4.2). Once behavior was characterized for homogeneous composite materials, these characterizations could be used in more sophisticated finite element analyses to predict the performance of the actual FGM structures.

A good understanding of the stress characteristics of the functionally graded TBC system is very important in the development of the fabrication processes and in the evaluation and ranking of various systems. The TBC thermal stresses can be minimized with proper selection of the individual layer thicknesses and compositions. In the design of FGMs,

both the residual stresses arising from cooling after processing, and the thermal and mechanical stresses generated by temperature gradients and constraints in the actual operating conditions, must be considered.

Large differences in thermal expansion characteristics and poor chemical compatibility of ceramics and metals result in low strength and durability of these materials. The FGM system permits a gradual change from the substrate to the fully ceramic portion of the FGM. The intermediate region can be designed with varying volume fractions, resulting in desirable profiles of thermal and mechanical properties. The effects of gradation size and material constants - such as Young's modulus, thermal conductivity, and thermal expansion coefficients - were investigated using finite element analysis, with graded properties assumed to follow rule of mixtures behavior.

One of the important tasks was to determine the optimum rate of these property variations for temperature and stress profiles. This requires a systematic and parametric study of the variables in the coating process that is beyond the scope of the proposed work, and is really application-specific. Our experimental and modeling characterization of selected FGM structures can provide a scientific framework for future engineering optimization. In the modeling study, the effects of different sizes of graded zones on the residual and thermal stresses were investigated.

Kaya et al. [81] provides an extensive literature review on TBC failure and life prediction. We have performed property estimation, heat transfer and stress analyses, with more detailed failure analyses being appropriate when a FGM system is eventually selected. Reducing the stress levels is only one function of the FGM coating [51]. Its second important function is to maintain an effective thermal protection. To determine the effects of microstructure, the heat transfer and stress analysis problems must be considered simultaneously and the functional distribution of the volume fractions must be varied through the thickness.

4.4 Thermal Conductivity of Nanocrystalline Ceramics

To understand the effects of nanocrystalline ceramic materials on thermal conductivity and structural stability, we concentrated on bulk nanocrystalline samples.

Ultrafine ZrO2-3 mol%Y2O3 powders were synthesized by chemical co-precipitation from chloride salts using our established procedure [84]. This synthesis technique produces relatively large amounts of powder (~20 g/batch) with a highly controllable particle size (ranging monotonically from 8 to 20 nm, depending on the pH used in the precipitating solution [67] and reproducibly high purity (<0.012 wt% oxide impurities) [85]. Most important, the powders are very weakly agglomerated, which means that they can be sintered to full density and still retain a grain size under 100 nm [67]. (In contrast, strongly agglomerated powders usually produce grain sizes on the order of the agglomerate size when they are densified; thus, even though the powder is nanocrystalline, the bulk samples produced from the powder have submicron- or micron-sized grains.) The ZrO2-3 mol%Y2O3 powders were processed into bulk samples for thermal diffusivity measurements. The bulk samples were made by techniques to vary the pore size/grain size ratio among the samples. It has been shown [73] that the starting powder packing arrangements, which are established by the consolidation technique, set the subsequent pore size evolution during sintering of the solid. Three candidate consolidation techniques were centrifugal casting of powder suspensions, sinter-forging of powder compacts, and pressureless sintering of powder compacts. All three techniques have previously been used in the laboratory facilities at Pennsylvania State University that were also available to the current program, and are explained more thoroughly in [86,87,73], respectively.
Using the above consolidation techniques, we attempted to achieve grain sizes ranging from 30 to 150 nm, with pores ranging in size from a few angstroms to 10 nm and densities from 63 to 100 percent, respectively. The varying grain-sized full-density samples would allow us to establish the role of grain boundaries in phonon scattering (or the establishment of conduction along a new grain boundary 'phase' if the two-phase mixture speculations are true). Similarly, a selection of samples with a wide range of pore sizes, but a given grain size and density, would allow us to determine more precisely the thermal conduction role of pores. For comparison to more standard zirconia ceramics, we also fabricated samples from commercial, submicron ZrO2-3 mol%Y2O3 (TZ-3Y powder from the Tosoh Co., in Tokyo, Japan; this powder is the finest commercial ZrO2-3mol%Y2O3, and its purity is currently comparable to that of our laboratory powders).

To measure grain sizes in our samples, we used x-ray line broadening (XRLB) with the results analyzed by the Scherrer technique [88]. Sample densities were measured by the Archimedes technique, and the sample pore size distribution was measured by nitrogen adsorption porosimetry and/or mercury intrusion porosimetry. For the smallest pores (<2 nm) - and in particular, for closed pores (which cannot be measured by either adsorption or intrusion techniques) - we could have used the small-angle neutron scattering and small-angle x-ray scattering (SANS and SAXS) facilities at the Oak Ridge National Laboratory, but decided this was not needed. Prior research has shown this technique to be quite valuable in measuring the pore size distributions of nanocrystalline materials [89], particularly under the restrictive conditions of very small pores and closed pores, as mentioned above.

Once the samples were manufactured and characterized, their thermal diffusivities were measured by laser flash thermal diffusivity at the Oak Ridge National Laboratory. The temperatures for thermal diffusivity measurements ranged from room temperature to 1000C. Because grain growth in pure ZrO2-3 mol%Y2O3 samples is known to occur at elevated temperatures [73], the microstructural characterization of high-temperature samples was performed after the thermal diffusivity measurements. From the thermal diffusivity results, the thermal conductivity can be calculated according to

$$K = d \rho C_P \qquad (4.4\text{-}1)$$

where K is the thermal conductivity, d is the thermal diffusivity, ρ is the sample density (which we measured by Archimedes' technique) and C_P is the sample heat capacity. The heat capacity was measured independently using differential scanning calorimetry (DSC) with Al2O3 as the reference material.

The data that resulted from these experiments was analyzed to yield thermal conductivity (and thermal diffusivity) as a function of grain size (or, equivalently, grain boundary density), pore size, and sample density. From the dependencies on these parameters, we were able to determine if new phonon scattering mechanisms are operative, or if two-phase conduction is present. Two-phase conduction is expected in the case of porous samples, where heat can be conducted both through the lattice and along the pores. As mentioned earlier, two-phase conductivity may exist even in dense samples, if the grain

boundaries are sufficient in number (note that for a 5-nm grain size sample, almost half the atoms will lie on grain boundaries) and sufficiently different in character from the lattice that they can be thought of as a second phase, distinct from the lattice. This two-phase conduction in dense, grain-boundary-rich material was first postulated by Charvat and Kingery many years ago [71], but to our knowledge, has never been observed.

5.0 Results and Discussion of Research

The research performed to characterize the high-conductivity, all-metallic expansion-graded bond coat to be coupled to the low-conductivity nanoceramic FGM TBC system is presented in this section. The work will be reviewed in terms of 1) the model and the bond coat components, 2) the fabrication of a representative FGM bond coat, and 3) the thermal properties of the nanoceramic structures.

5.1 Modeling and Candidate Bond Coat Behavior

System concepts were surveyed to decide on a material system to model and to characterize experimentally. Some of the systems considered consisted of superalloys and NiAl or (Ni,Pt)Al, combined with: refractory monocarbides (Ta,Ti...)C; bcc metals W, Mo, Cr; oxidation resistant carbides such as CrxCy; intermetallic phases such as Cr3Si or Cr2Ta; combinations of the above.

Systems which used either refractory metal W or Mo to reduce CTE while maintaining or increasing conductivity were removed from consideration because these elements in the fractions (0.2-0.3) needed to provide sufficient expansion reduction would severely degrade oxidation resistance to unacceptable levels. These would also add substantially to airfoil mass. Systems relying on the monocarbides of Ta, Ti, Nb, V, Hf and Zr all can be in equilibrium with superalloys. However, these were removed from consideration due to their dramatic degradation of environmental resistance. Some of these systems could result in significant density reductions, contributing to lighter coatings. These materials could prove valuable in controlling expansion and conductivity, provided they were buried beneath the surface. Coating structures combining an outer protective layer over these less resistant materials could make an acceptable FGM.

The intermetallic phase Cr3Si is an interesting candidate. It has a high-temperature equilibrium with NiAl, but can reduce the temperature capability of the underlying substrate if it reacts to form lower melting silicides that are in equilibrium with the superalloy. This material was not modeled due to these concerns, but concepts are possible where this phase is isolated in the NiAl to provide a useful combination of properties.

The selection was finally narrowed to structures of NiAl and the Ni solid solution (Ni,...) with different contents of α-Cr and the M7C3 (Cr-rich M) phase. This material family offers light weight, good oxidation resistance, and a range of mechanical and physical behaviors. The modeling and experiments considered only β based on NiAl, but could have easily treated β phases modified by Pt for enhanced oxidation resistance.

The alloy candidates for the different regions of the FGM are listed in Table 5.1. These can be put in context by the schematic phase diagrams in Figure 5.1. The alloys contained different fractions of the phases M7C3, (Ni,...), β, and α-Cr. Since (Ni,...) and NiAl are relatively high in CTE, similar to the single crystal superalloy, they were the predominant phases for the region of the FGM closest to the substrate. A single alloy (alloy 7 in the table) was selected for the study for that innermost layer. The location of that alloy is represented in phase space in Figure 5.1. For regions somewhat removed from the substrate, two alloys were selected. Both had 15% each of α-Cr and M7C3, with alloy 5 having more (Ni,...) than NiAl, and alloy 6 having the opposite phase distribution. These materials would thus have different Al levels to re-supply Al to the surface as oxidation and spallation proceed. This is not an issue while the TBC ceramic remains in place, since the thermally grown oxide (TGO) growth rate decreases rapidly for the parabolic growth kinetics in the absence of spalling. Once the TBC ceramic is lost, the coating must provide protection for the underlying substrate, so that aluminum availability is important. Again, the alloy 5 and 6 chemistries are represented in Figure 5.1. The microstructure of alloy 2 is included in Figure 5.1.

Table 5.1 - Candidate Alloy Compositions for FGMs (phase v/o and alloy elemental a/o)

	α	β	γ	M_7C_3	Ni	Cr	Al	C
1	45	25	30	0	36.5	51.1	12.4	0
2	30	25	30	15	37.8	45.4	12.3	4.5
3	15	25	30	30	39.2	39.7	12.1	9.0
4	0	25	30	45	40.5	34.0	12.0	13.5
5	15	25	45	15	48.2	33.7	13.6	4.5
6	15	45	25	15	46.2	30.5	18.8	4.5
7	0	25	60	15	58.5	22.0	14.9	4.6

α-98Cr 1Ni 1Al; β-4Cr 60Ni 36Al; γ-20Cr 70Ni 9.9Al 0.1C; M_7C_3-60Cr 10Ni 30C (a/o)
[approximate phase chemistries at 1100 °C]

For the region of the FGM immediately below the ceramic, the lowest CTE is desired, with Al concentration sufficient to maintain alumina growth. Four alloys (1-4 in Table 5.1 and Figure 5.1) were selected for evaluation. These have a sum of 45% of the low-expanding α-Cr and M7C3, with each of those phases varying between 0 and 45%. The remainder of this region is (Ni,...) and NiAl sufficient to provide an Al level to support alumina growth.

For the modeling work, properties were estimated for each of these 7 layer chemistries based on rule-of-mixtures. The estimates are shown as functions of temperature in Figure 5.2. Included in the figures are properties typical of YS-zirconia and of Rene N5, an advanced single crystal superalloy. The Rene N5 is used with the low-modulus [100] crystallographic direction in the plane of the airfoil wall. The modulus in Figure 5.2 is thus much lower than values shown for the FGM materials, which are equiaxed (Ni,...), NiAl, and the stiffer α-Cr and M7C3.

The case study model is illustrated in Figure 5.3. The cooling air and combustion gas temperatures and heat transfer coefficients result in predictions which are consistent with expected metal and TBC temperatures. The zirconia layer is isolated from the superalloy substrate by three layers of the FGM bond coat, BC1, BC2 and BC3. In all case studies, BC3, nearest the substrate, was assumed to have the properties of alloy 7. The

intermediate layer BC2 was either alloy 5 or 6, and the surface layer BC1 was either alloy 1, 2, 3 or 4. This gave a substantial range of elastic modulus variation while essentially maintaining expansion behavior unchanged from alloy to alloy. The thermal conductivities were generally greater for the FGM than for the highly alloyed superalloy substrate (Figure 5.2). For case study identification, the labeling convention employed, by example, was **A15**, where the layer thicknesses were those of case type **A** (see Figure 5.4), BC1 was alloy **1**, and BC2 was alloy **5**, BC3 was always alloy 7, and therefore did not need to be specified in the label.

Figure 5.4 illustrates the different cases, where the total thickness of BC1, BC2, and BC3 summed to 0.1 mm (100μm), but where the inner and outer layer thicknesses were varied from 0.025 to 0.045mm, while BC2 was always 0.030mm. The ceramic thickness and substrate thickness were held constant at values typical of aircraft engine blade airfoil walls.

Modeling of FGM Systems - Twenty-four elastic cases were run in the FGM finite element analysis of thermal stresses generated in a cooled structure in a hot gas (thermal stress assumed to be zero at room temperature). In addition, some calculations were performed on monolithic bond coat structures.

To a first approximation, the TBC surface temperature was 1200°C, the bond coat/TBC interface was 965°C, the bond coat/superalloy interface was 954°C, and the cold wall of the superalloy was 810°C. These temperatures varied by +/-3C. Base cases were also calculated for an all-β bond coat in the case studies, varying elastic modulus from values equivalent to the single crystal substrate to values of alloy 6. In real airfoils, the β phase can be fine equiaxed grains, or it could be a single grain across the thickness, which may or may not have a preferred texture. Temperatures calculated for the base cases were as above for the FGMs. When a graded alumina-MCrAlY case was calculated, the temperature at the TBC/bond coat interface was approximately 10C higher than for the all-metallic bond coat calculations.

The range in elastic modulus and expansion behavior assumed for alloys 1-4 resulted in calculated elastic stresses varying from ~250MPa to ~400MPa, as seen in Figure 5.5. These stresses would be substantially reduced in an elastic-plastic analysis. For

monolithic β bond coats, the stresses calculated for the TBC layer were strongly dependent on the assumed modulus. The calculation labeled BASEX in Figure 5.5 was for modulus equivalent to the single crystal substrate. When the higher modulus values were used, results of the TBC stress calculation matched A15-A16 in Figure 5.5. If actual values were used in the case study calculations, based on our measured expansion and room temperature modulus values, the four BC1-layer alloys 1-4 are expected to be closer in stress state, and possibly to be less stressed due to their lower actual moduli. However, the high-Cr alloy is expected to reduce stresses plastically much further than the high-M7C3 alloy 4, because of differences in strength and ductility between these two materials.

The calculated stresses in the YSZ TBC, ~25MPa, are about 20% lower than the calculated value for the TBC on a monolithic coating on a single crystal superalloy. This amount of reduction may be significant in reducing the driving force for TBC loss due to alumina spallation or TBC delamination.

Materials for FGM Bond Coats - All seven of the FGM alloys were produced by induction melting and casting, and were directionally solidified at 20cm/h to produce sound material, and test pins 2.5 cm long and .25 cm in diameter were taken in a transverse orientation to produce a multi-grained, non-directional sample axis for dynamic modulus, dilatometric thermal expansion and oxidation. A pin of each was tested in one-hour cyclic oxidation to 1100°C for 525 hours.

Pin samples were subjected to differentialdilatometric evaluation over the range 23-1200°C, with a heating rate of 10°C/min, with an alumina standard. Rule-of-mixture estimates of thermal expansion were made before testing, by using known data for the three metal phases and their expected volume fractions, and using an assumed expansion behavior for the carbide that was somewhat lower than that of Cr (~0.85 x % expansion of Cr). These estimated values predicted expansion of ~1.4% (1.38% for alloy 4, 1.45% for alloy 1) from room temperature to 1100°C. These values are all greater than the 1.22% expansion of YSZ. However, the measured expansion showed the carbide-free alloy 1 to be lower in expansion than expected, and quite close to YSZ. The carbide-containing

alloys 2-4 showed substantially greater expansion than expected, and greater than alloy 1 or YSZ (Figure 5.6). Small differences in the volume percentages of the low-expansion αCr and/or carbide phases from those assumed in Table 5.1 could account for the differences in expansion behavior. All four alloys exhibited markedly increased rates of expansion above 1000°C. At approximately this temperature, there is a four-point invariant reaction in the NiCrAl equilibrium diagram. At temperatures greater than 1000°C, there is a γ-β phase field that isolates γ' from α, while below that temperature the α-γ' field replaces the γ-β field. As temperature rises above 1000°C, the volume fraction of α in the structure is reduced, and the suppression in expansion behavior of the alloys due to the αCr phase is lessened. Elastic modulus measurements were made at room temperature using a dynamic ultrasonic method. Values of 241-248 GPa were estimated, based on values of 290-310 GPa for the Cr and carbide phases, and values of 193-207 GPa for γ and β. Measured values were 221-228 GPa for alloys 1-4, with the range too small to see any trend.

Pin samples .25cm in diameter and 2.5 cm in length were subjected to one-hour cyclic oxidation in a static air furnace, with periodic removal for visual evaluation and weight measurements. Weight gain per unit area is shown in Figure5.7, along with a microstructure for oxidized alloy 2 Oxidation rate is relatively low for alloy 1, and rate of oxidative attack is seen to increase with carbide volume fraction. Samples were continued through 525 hours of cyclic oxidation, with alloy 1 showing a gain of 14.5 mg/cm^2, alloy 2 a loss of 17.6, alloy 3 a gain of 16.3, and alloy 4 a gain of $72mg/cm^2$. For reference, if a weight gain reflected only growth of M_2O_3, with no simultaneous spallation, a weight gain of ~$2mg/cm^2$ would represent 10μm of oxide growth. If a weight loss reflected only spallation of oxide, with no simultaneous oxidation, a weight loss of ~$7mg/cm^2$ would represent 10μm of metal loss to oxide spallation. Alumina formation resulted in substantial Al depletion. The alumina scale is not protective, and loss of β phase due to Al diffusion to the surface oxide growth front is evident, as is internal oxidation where the Al loss has been greatest. For reference, formation of 10μm

of alumina consumes >10μm of NiAl, >27μm of a 20a/o Al alloy, and >50μm of a 10a/oAl alloy.

Summary of Modeling and Candidate Bond Coat Behavior

It appears possible to essentially match the expansion behavior of YSZ TBCs using alloys which are combinations of metal phases αCr, βNiAl, and γNi. Building gentle gradient structures in all-metallic materials can involve simple variation of the proportion of α phase through the thickness of the FGM. It may be necessary to modify FGM microstructures and chemistries to promote better oxidation resistance (a richer Al source within the FGM), and to develop greater phase stability if TBC/FGM interface temperatures exceed 1000°C. The possibility of stress reduction in the TBC in such a material system is very promising.

5.2 Fabrication of FGM Structures

The creation of a controlled graded chemistry for the bond coat portion of the FGM presents several possible difficulties. The aerodynamics of the throat area of the high pressure turbine in jet engines dictate that the graded structure be produced in essentially the same thickness as current conventional bond coats, on the order of 50 to 100 microns. This makes powder processing difficult, since the powder sizes of the metallic bond coats are typically distributed about a mean of 20-25 microns, to avoid (O, N) contamination of the large surface-to-volume ratios for finer powders. Even for thermal spray processed powders, splatted particle sizes are on the order of 10 microns in thickness, so that only a few layers of particles can be contained within the required coating thickness, severely limiting the process and the gradient control that is achievable.

Physical vapor deposition processes offer the possibility of building gradients. Multiple-target sputtering systems, or multiple-pool electron beam evaporation systems both can produce gradients in thin sections. This is accomplished by alternating the exposure of the surface being coated from one source to a second in a controlled fashion, either by physically moving the target or substrate, or by energizing one then the other deposition source. For coating systems with more than two elements, such as in the polycomponent

FGMs, further difficulties can arise from differing vapor pressures or differing sputter rates for the multiple elements being deposited.

Graded structures have been produced by EBPVD from a single pool [57]. By using a fixed-volume deposition source and consuming that source in the evaporation process, the differential vapor pressures can be used to create the graded chemistry directly. In Movchan's experiments, a fixed volume of Al-based source material was placed in a continuous feed-rod crucible, above a feed-rod of zirconia. The high-vapor-pressure Al evaporated more rapidly than the other solute elements initially, leaving an increasingly solute-enriched liquid pool above the zirconia feed-rod. Gradually, the other elements were also evaporated as the Al was depleted, until only the zirconia remained to evaporate at even lower rates. In these experiments, the gradient in chemistry was produced over a very thin region, generally less than 5 microns.

In our experiments described below, for both binary and more complex structures, larger fixed-volume sources were used, evaporating from tungsten crucibles held in water-cooled Cu hearths, to produce graded structures of approximately 25 microns thickness, which when reacted with the superalloy substrate, produced coatings of 50 microns thickness.

Binary Deposits

The experiment is shown schematically in Figure 5.8. A homogeneous Al-base material was placed in the tungsten crucible and evacuated to $<10^{-6}$ torr. The electron beam was then directed onto the source material. For the Al-base alloys, 5 minutes at 0.5kW produced melting with little evaporation. Then, in two-minute cycles, the power to the pool was increased to 1, 1.5, 2 and 2.5KW, with the pool being essentially fully consumed by evaporation at the end of this cycle.

The vapor pressure as a function of temperature is plotted for pure Al and pure Si in the figure. For the pure-element cases, at temperatures of interest, the Al vapor pressure is 10-1000 times greater than is the Si vapor pressure. The figure also shows schematically the liquidus temperature varying from 660C for pure Al at the left of the plot, to 1414C

for pure Si at the right of the plot, with a eutectic of 577C at the Al-rich end of the binary system.

As the evaporation begins from the pool at a power level of 1KW, for a pool of nominally 10a/o Si, the evaporant is nearly pure Al, since the pure-element ratios of vapor pressure are approximately 1000:1. During the two minutes at 1KW, the pool is becoming more enriched in Si as Al is evaporating preferentially. As power is increased through 1.5 and 2KW to 2.5KW, Si is evaporated at a significant rate, due to the higher pool temperature and the Si-richer pool chemistry. The figure also shows schematically the graded AlSi deposit on the substrate supported above the pool in the vapor cloud.

The experiments can be carried out with heated substrates, in which case reactions between the deposit and the substrate occur in situ, producing the final coating directly. However, this also leads to diffusional fluxes that mask the degree of gradation produced by the process, as homogenization occurs. For the experiments performed in this study, substrate temperature was maintained below 550C to avoid a liquid deposit and substantial reaction with the substrate. There was some Ni diffusion into the deposit, even at these low temperatures, which led to some brittle phase formation. This procedure still led to the best determination of gradient formation in deposition, and subsequent heat treatment could be performed to form the reacted coatings.

Pure-element vapor pressures as functions of temperature are shown in Figure 5.9 for Al, Cr, Si and Zr. For binary pools the vapor pressure differentials are about a factor of 10 for Al and Cr; Al-Si was discussed above; for Al-Zr the differential is six orders of magnitude for the pure elements. These elements were chosen since they represent an extremely wide range of pressure differentials relative to Al, so that the expected range of chemistries which might be considered for bond coatFGMs might conceivably have differentials as wide as displayed by the selected binaries.

Also shown in Figure 5.9 are the deposit chemistries as a function of distance from the substrate, for Cr, Si and Zr evaporated from the Al-rich binary source ingots. Nominal chemistries of the ingots were Al-10a/oCr; Al-10a/oSi; and Al-0.5a/oZr. For each binary, as expected, the initial deposit was much poorer in solute concentration than was the source ingot. The 22 micron thick Al-Cr deposit had chemistry varying from about 1a/oCr initially, to about 40a/oCr in the last material deposited. The 24 micron thick AlSi deposit varied from about 0.1a/oSi adjacent to the substrate, to again about 40a/o Si. The 16 micron thick Al-Zr deposit varied from nil Zr adjacent to the substrate, to about 1a/oZr at the surface. The Al-Zr source ingot was not fully consumed during deposition, so that the remaining Zr-rich material may have required a higher evaporation power than was used in the experiment. Source ingots were ~16g for Al-Cr, ~15g for Al-Si and ~15g for Al-Zr, with pool-to-substrate distance maintained at 15cm.

For the binary cases, it is clear that gradients can be achieved. Surface chemistries and the rate of chemical grading are expected to be functions of the source ingot concentrations, total source volume, power levels, and the ramp rate in power. For example, a slower ramp rate or a constant low power level such as 1.5kW, will evaporate Al proportionately greater, so that the solute is more concentrated in the final deposition regime, once the source ingot is sufficiently rich in solute. If the power levels are too low, however, there may be insufficient heating to evaporate a significant quantity of the solute. This trend will increase as the solute selected is more refractory in terms of its vapor pressure - temperature relationship.

Complex Deposits

To extend the experiment to a more complex chemistry, an ingot was induction melted of nominally Al-10a/oCr-10a/oSi-x0.2a/oY. A source ingot of ~16g was prepared for evaporation, and the pool heating sequence was selected to be equivalent to that used for the binary alloys. The pure-element vapor pressure - temperature curves are shown in Figure 5.10. The schematic drawings indicate the gradient in chemistry from low-temperature deposition and the subsequent growth in coating thickness as the superalloy

substrate and graded coating are reacted to form NiAl from the Al in the deposit. The metallographic images are of the as-deposited material and theRene N5 substrate - graded coating reacted after deposition by a heat treatment of 1100C/4h/vacuum. The as-deposited material is chemically graded, but is quite brittle due to the very highCr and Si levels and to some interaction with the superalloy substrate even at these low temperatures. The cracking seen in the figure is believed to be from cutting and metallographic preparation, since macroscopic investigation of the deposit surface showed no evidence of cracking. After heat treatment, the formation ofNiAl is the primary phase adjacent to the superalloy substrate, while the outer regions of the deposit contain an appreciable concentration of Cr3Si in equilibrium withNiAl. Even through a heat treatment where liquation of the EBPVD Al-rich coating almost certainly occurred, a strong chemical gradient was achieved in the reacted coating.

Summary of Fabrication of FGMs

The possibility of deposition from a single source ingot of bond coats of graded chemistry was demonstrated clearly. The gradient was achieved in thicknesses totally compatible with aerodynamic requirements on coated jet engine components. Some homogenization occurred during reaction of the Al-rich deposits with the Ni-superalloy substrates, but continuous gradient microstructures still resulted from heat treatment. For practical coatings it may be desirable to deposit at a sufficiently high substrate temperature to achieve in situ reaction.

5.3 Thermal Properties of Nanocrystalline Zirconia

The discussion of the investigation of nanoceramicTBCs consists of three parts—experimental details, results and discussion, and summary of thermal properties.

Experimental Details

Nanocrystalline powders containing 0, 5.8, 8 and 15wt% yttria, corresponding to 0, 3.3, 4.5 and 8.8mol% yttria were synthesized by theco-precipitation method[84]. Commercially available 5.3wt.% (3mol%) yttria stabilized zirconia powder from TOSOH corporation, Japan, was also used in the present work. Powder characteristics are given in

Table 5.2. Crystallite sizes were measured by X-ray line broadening [58] using the 111 tetragonal peak. Particle sizes were measured on a Horiba CAPA-700 particle size analyzer which is based on a centrifugal photo-sedimentation technique. The TOSOH powders are made up of spray dried granules about 50μm in diameter which in turn is made up of agglomerates about 300nm in size. The primary crystallite size is of the order of 35nm though. The chemical compositions, in wt.%, of the 5.8wt% nanocrystalline and TOSOH powders were determined by inductively coupled plasma spectroscopy at CELS, Laboratory Services, Corning, New York and are listed in Table 5.3. It is expected that the trace element levels in the other nanocrystalline powders are similar to those of the 5.8wt.% composition since all nanocrystalline powders were produced under identical conditions.

Table 5.2: NanocrystallinePowder Characteristics

Powders	X-Ray Crystallite Size (nm)	Specific Surface Area (m2/g)	Mean Particle Size by Number (nm)	Mean Particle Size by Volume (nm)
Nanocrystalline (5.8 wt. %)	16	61	10	30
TOSOH	35	17	-	-

Table 5.3: Nanocrystalline Chemical Compositions

Constituents	Y_2O_3	SiO_2	Hf	Al, B,	Ca, Fe, Ni, Si	Cr, Mg, Pb
Nanocrystalline (5.8 wt. %)	5.88	0.041	0.3-1.0	.003-.01	0.001-0.003	<0.001
TOSOH	5.30	0.014	-	-		

All powders were compacted by uniaxial pressing without a binder. The green bodies were sintered in air to yield disc shaped samples approximately 12 to 14 mm in diameter and 0.6 to 1mm in thickness. The sintered densities of the 5.8wt.% nanocrystalline samples were varied from 63 to 100% (based on a theoretical density of 6.1 gm/cm3 for the tetragonal powders) and the grain sizes from 30 to 150nm by using various

combinations of sintering time (0.5-15 h) and temperature (1000-1150°C). All other powders were sintered at times and temperatures (1300°C for TOSOH and 15wt.% zirconias and 1150°C for 0wt% and 8wt.% zirconias) necessary to produce near theoretical density. Grain sizes less than 100 nm were determined from the peak widths of the 111 tetragonal peak and the $\bar{1}11$ monoclinic peak using the Scherrer equation. The phase compositions in wt.% of the 98% dense sintered samples determined by X-ray diffraction using the integrated intensities of the relevant peaks. Sintered densities ρ, were measured by the Archimedes technique.

Samples used for specific heat capacity measurements, 4 mm diameter and 1.5 mm thickness, were fabricated out of fully dense, disc shaped samples by using a diamond tipped core drill.

Thermal diffusivities, α, were measured by the laser flash technique[59] at the Oak Ridge National Laboratory on a Flashline 5000 Thermal Diffusivity System, (Anter Corporation, Pittsburgh, Pa). Prior to measuring thermal diffusivity, the samples were sputter coated with 1000Å of platinum or gold-palladium alloy to make them opaque and then with a thin layer of colloidal graphite to ensure complete and uniform absorption of the laser pulse and similar surface radiative characteristics in all the samples. All the measurements were carried out from 100 to 1000°C in 100 degree intervals, in nitrogen. Three samples were used for each combination of density and porosity, and three measurements were made at every temperature. The time-temperature curves were analyzed by the method of Clark and Taylor, [90] which takes into account radiation losses and uses the heating part of the curve to calculate thermal diffusivity. Specific heat capacities, C_P, were determined in the temperature range of 100-1000°C by differential scanning calorimetry on an Omnitherm DSC 1500 using sapphire as the baseline standard.

The thermal diffusivity, specific heat and density were used to calculate the thermal conductivity (**k**) according to,

$$\mathbf{k} = \alpha \rho C_P \qquad (5.1)$$

Finally, powders containing 5.8, 8 and 15 wt. % yttria were pressed into disc shaped samples with a green density of about 50% of theoretical density and were aged in air at 1000°C for up to 1000 hrs.

Results and Discussions:

Phase Composition: The phase compositions of the nano-powders in wt.% used are listed in Table 5.4. The TOSOH powders were 100% tetragonal.

Table 5.4: Phase Compositions

Wt % Y_2O_3	0.0	5.8	8.0	15
Monoclinic	100	-	-	-
Tetragonal	-	100	77	-
Cubic	-	-	23	100

Specific Heat Capacities: The specific heat capacity vs. temperature curves for the samples in Table 5.4 and samples made out of the TOSOH powders are plotted in Figure 5.11. These values are similar to the specific heat values of EB-PVD and APS TBC's in literature [91] This indicates that the specific heat is insensitive to microstructure.

Effect of Grain Size, Porosity and Temperature on Thermal Conductivity of 5.8 wt. % YSZ:.The effects of varying grain size, porosity level and temperature on the thermal conductivity of the 5.8wt.% yttria stabilized nanocrystalline tetragonal zirconia are summarized in Figure 5.12. There is almost no effect of temperature on thermal conductivity except for the 63% dense sample in which the slight increase in thermal conductivity at temperatures above 600°C is attributed to strong radiation contributions because of the porosity. Data fall in groups by the porosity level and not the grain size. Within each porosity level there appears to be no discernible effect of varying the grain size. Problems with sample fabrication and the fact that it is not possible to entirely separate grain growth and densification during sintering prevented the variation of sintered density at lower grain sizes. Hence, it cannot be said with certainty if the absence of grain size effects extends down to 30 nm and below. While the temperature independence is typical of the thermal conductivity of stabilizedzirconia,[92] which is strongly dominated

by oxygen vacancy scattering, the present study shows that this scattering mechanism is so dominant that grain sizes as low as 50 nm are ineffective in causing any additional reduction in conductivity.

As can be seen from the same Figure, porosity has a significant effect on reducing the thermal conductivity. In order to determine whether the entire drop in conductivity is due only to porosity effects, a composite model, Equation 5.2, was used.

$$K = k_{solid} V_{solid}^{3/2} + k_{pore} V_{pore}^{1/4} \quad (5.2)$$

This equation, which is an interpolation formula, relates the effective thermal conductivity of the composite, **k**, to the thermal conductivities of its constituent solid and pore phases and their volume fractions, **V**. The model [93] is valid in the whole range of porosity for a two phase structure with a continuous solid phase and homogeneously distributed porosity, as was the case in the samples used. The thermal conductivity data for the dense tetragonal zirconia samples were used for k_{solid}. This was done only on data gathered at 100°C to avoid the complications arising out of radiation contributions as much as possible. In the absence of radiation contributions, k_{pore} in the second term, whose effect is negligible, could vary between zero to the thermal conductivity of nitrogen. The results of the calculations, with k_{pore} taken as zero, are compared with measured values in Figure 5.13. The measured values of thermal conductivity are still lower than those predicted by the above model and the difference increases with reducing bulk density. The reason for this difference is not clear. Significant errors associated with the measurements of V_{solid} and V_{pore} in individual samples are unlikely and the value assigned to k_{pore} is at its most conservative. A possible explanation for the lower measured values is that the thermal conductivity of the solid phase in low density samples is for some reason less than that of the fully dense solid—perhaps due to incomplete bridging between neighboring particles or the complex morphology of the pores.

Effect of Yttria Content on the Thermal Conductivity of YSZ: The effect of yttria content on the thermal conductivity vs temperature plots is shown in Figure 5.14. Atomic defect

scattering, as in the tetragonal zirconia of Figure 5.12, is responsible for the insensitivity of thermal conductivity to temperature in the 8 and 15wt.% yttria samples. At a given temperature, the decrease in thermal conductivity with larger yttria contents is consistent with oxygen vacancies playing the dominant role in phonon scattering. It is noteworthy that while there is a relatively large drop in conductivity in going from 5.8 to 8wt.% yttria, a further increase in yttria content to about 15wt.% does not cause a proportionate decrease in conductivity. The thermal conductivities for the monoclinic zirconia were calculated using values of specific heat from the literature [94]. It is stressed that the monoclinic zirconia is pure zirconia with a grain size of 63 nm, with no stabilizer additions and having impurity contents similar to the indigenously produced 5.8wt.% nanocrystalline tetragonal zirconia. The strong temperature dependence of thermal conductivity in the monoclinic material shows that even in the absence of oxygen vacancies, defect scattering is not the dominant mechanism. The thermal conductivity of monoclinic zirconia has been re-plotted in Figure 5.15 against 1/T. The linear variation ofk with 1/T is characteristic of phonon scattering by Umklapp processes (phonon-phonon scattering) above the Debye temperature (about 230° C for zirconia [95]). This suggests that even in the absence of defects a grain size of 63nm is still not sufficiently small to observe any grain boundary scattering effects.

Data from the present work has been compared with thermal conductivity of APS and EB-PVD yttria stabilized zirconia coatings from the literature in Figure 5.16. It can be seen that the thermal conductivities of 96% dense 8wt % yttria stabilized zirconia are only slightly higher than that of the EB-PVD coating with 7wt% yttria despite the fact that the latter has a density of only 84% (theoretical densities are 6.056 gm/cm3 and 6.049 gm/cm3 for the 8wt.% and 7wt.% compositions respectively [96]). Given the large impact of porosity on conductivity, it is expected that a reduction in the bulk density of the nanocrystalline 8wt% yttria stabilized zirconia to about 80% should yield values of conductivity lower than the EB-PVD coatings. Another factor that needs to be considered is that both the EB-PVD and the APS coatings are susceptible to an increase in conductivity on thermal aging, though compared to the APS coatings, EB-PVD coatings are more resistant to this phenomenon. Even though the APS coatings have low initial

conductivity, after aging at 1000°C for 1000 hours their thermal conductivities increase by as much as 1.6 times the original value. The potential thus exists for developing porous, nanocrystalline yttria stabilized zirconia coatings with conductivities lower than that of the presently available coatings. However, their success would also depend on an increased resistance to thermal aging.

Thermal aging The change in density (gm/cm3) with time at 1000°C for the various YSZs is tabulated below. As expected samples made with the TOSOH powder, smaller specific surface area and hence lesser sinterability, are more resistant to aging as compared to samples made with nanopowders. It is also interesting to note that the cubic nanocrystalline YSZ (15 wt % Y2O3) powders are more resistant to aging than the nanocrystalline 5.8 wt. % Y2O3 powders in spite of having similar starting powder characteristics.

Table 5.5: Effect of Aging of Nanocrystalline at 1000°C on Relative Density

Time	24 hours	250 hours	500 hours	1000 hours
grain size, 5.8wt% YSZ nanocrystalline	69nm	84nm	85nm	88nm
grain size, 5.6wt% YSZ TOSOH	51	56	56	56
grain size, 15wt% YSZ nanocrystalline	54	68	72	72

Summary of Thermal Properties

Thermal conductivity of dense 5.8wt% YSZ is independent of grain size between about 400 nm and 70 nm. Thermal conductivity at grain sizes >/= 50 nm is dominated by oxygen vacancy scattering and porosity effects.

Reduction in conductivity with bulk density of 5.8wt.% YSZ is largely due to porosity but may have non-grain-size-related contributions from the solid phase.

The thermal conductivity of nearly dense pure monoclinic is dominated by the Umklapp process (phonon-phonon scattering),and not defect scattering in spite of a very small grain size (63nm).

Structures produced from the TOSOH and 15 wt. nanocrystalline YSZ powders are more resistant to thermal aging than are structures from the 5.8 wt. nanocrystalline YSZ powders.

6.0 Summary of Technical Results

FGM Materials Properties and Modeling

- It appears possible to essentially match the expansion behavior of YSZTBCs using alloys which are combinations of metal phases αCr, βNiAl, and γNi.
- Building gentle gradient structures in all-metallic materials can involve simple variation of the proportion of α phase through the thickness of the FGM.
- It may be necessary to modify FGM microstructures and chemistries to promote better oxidation resistance (a richer Al source within the FGM), and to develop greater phase stability if TBC/FGM interface temperatures exceed 1000°C.
- The possibility of stress reduction in the TBC in such an FGM material system is very promising.

Fabrication of FGMs

- The possibility of deposition from a single source ingot of bond coats of graded chemistry was demonstrated clearly.
- The gradient was achieved in thicknesses totally compatible with aerodynamic requirements on coated jet engine components
- Some homogenization occurred during reaction of the Al-rich deposits with the Ni-superalloy substrates, but continuous gradient microstructures still resulted from heat treatment.
- For practical coatings it may be desirable to deposit at a sufficiently high substrate temperature to achieve in situ reaction.

Thermal Properties of Nanocrystalline Zirconia

- Thermal conductivity of dense 5.8wt% YSZ is independent of grain size between about 400 nm and 70 nm.
- Thermal conductivity at grain sizes >/= 50nm is dominated by oxygen vacancy scattering and porosity effects.
- Reduction in conductivity with bulk density of 5.8wt.% YSZ is largely due to porosity but may have non-grain-size-related contributions from the solid phase.

- The thermal conductivity of nearly dense pure monoclinic is dominated by the Umklapp process (phonon-phonon scattering),and not defect scattering in spite of a very small grain size (63nm).
- Structures produced from the TOSOH and 15 wt. nanocrystalline YSZ powders are more resistant to thermal aging than are structures from the 5.8 wt. nanocrystalline YSZ powders.

7.0 References

[1] M.J. Mayo, 'Superplasticity of Nanostructured Ceramics,'Mechanical Properties and Deformation Behavior of Materials Having Ultrafine Microstructures, M. Nastasi, D. Parkin, and H. Gleiter, ed., Dordrecht, The Netherlands, Klewer, pp. 361-380 (1993).

[2]H. Hahn and R.S. Averback, 'Low Temperature Creep of Nanocrystalline Titanium(IV) Oxide,' J. Am. Ceram. Soc. 74, pp. 918-21 (1991).

[3]D.J. Wortman, B.A Nagaraj and E.C. Duderstadt, Mat. Sci. Eng. A121, p. 433 (1989).

[4]R.A. Miller, Surface and Coatings Technology 30, p. 1 (1987).

[5]R.A. Miller, J.L. Smialek and R.G. Garlick, Advances in Ceramics, Vol. 3, Science and Technology of Zirconia, The American Ceramic Society, p. 241 (1981).

[6]D.P.H. Hasselman, L.F. Johnson, L.D. Bentsen, R. Syed, H.L. Lee and M.V. Swain, Ceramic Bulletin 66. p. 799 (1987).

[7]N. Iwamoto, Y. Makino and Y. Arata, Proc. Int. Thermal Spraying Conf., The Hague, Netherlands, p. 267 (1980).

[8]H. Nakahira, Y. Harada, N. Mifune, T. Yogoro and H. Yamane, Proc. Int. Thermal Spray Conf., Orlando, FL, p. 519 (1992).

[9]G. Johner and K.K. Schweitzer, Thin Solid Films119, p. 301 (1984).

[10]S. Stecura, Thin Solid Films 150, p. 15 (1987).

[11]S. Stecura, NASA Technical Memorandum 86905 (1985).

[12]Ch. Meterns-Lecomte, D. Muck and J. Garcia, Proc. 7th Int. Thermal Spray Conf., Boston, MA, p. 61 (1994).

[13]P.A. Siemers and R.L. Mehan, Ceramic Eng. & Sci. Proc., Vol. 4, p. 828 (1983).

[14]S.M. Meier, D.M. Nissley, K.D. Sheffler and T.A. Cruse, Trans. ASME 114, p. 258 (1992).

[15]S. Stecura, Thin Solid Films 136, p. 241 (1986).

[16]P. Sahoo and R. Raghuraman, Proc. 1993 National Thermal Spray Conf., Anaheim, CA, p. 369 (1993).

[17]R.A. Miller and C.E. Lowell, Thin Solid Films 127, p. 129 (1985).

[18]T.E. Strangman, Trans. ASME 114, p. 264 (1992).

[19]J.W. Watson and S.R. Levine, Thin Solid Films 119, p. 185 (1984).

[20]G.D. Smith, J. Eng. for Gas Turbines and Power 113, p. 135 (1991).

[21]R.A. Miller, W.J. Brindley, J.G. Goedjen, R. Tiwari and D. Mess, Proc. 7th Int. Thermal Spray Conf., Boston, MA, p. 49 (1994).

[22]J.R. Rairden, GE-CRD Report No. 90CRD236, Schenectady, NY (1991).

[23]J.R. Rairden and D.M. Grey, GE-CRD Report No. 90CRD233, Schenectady, NY (1991).

[24]H.E. Eaton and R.C. Novak, Ceramic Eng. & Sci. Proc., Vol. 7, p. 727 (1986).

[25]J. Musil, J. Filipensky, J. Ondracek and J. Fiala, Proc.Int. Thermal Spray Conf., Orlando, FL, p. 525 (1992).

[26]S.L. Shinde, D.A. Olson, L.C. DeJhonge and R.A. Miller, Proc. 10th Ann. Conf. Composites and Advanced Ceramic Materials, Am. Ceram. Soc., Columbus, OH, p. 1032 (1986).

[27]E.Y. Lee and R.D. Sisson, Jr., Proc. 7th Int. Thermal Spray Conf., Boston, MA, p. 55 (1994).

[28]B-C. Wu, E. Chang, S-F. Chang and C.H. Chao, Thin Solid Films 172, p. 185 (1989).

[29]A.M. Ritter, J.R. Rairden and R.L. Mehan, Mat. Res. Symp. Proc., Vol. 190, p. 7 (1991).

[30]C.C. Berndt, J. Ilavsky and J. Karthikeyan, Proc. Int. Thermal Spray Conf., Orlando, FL, p. 941 (1992).

[31]C.H. Leibert and S. Stecura, 'Thermal Barrier Coating System,' U.S. Patent 4,055,705, October 25,1977.

[32]R.D. Dowell, 'Coating for Metal Surfaces,' U.S. Patent 3,911,891, October 14, 1975.

[33]G.W. Goward, D.A. Grey, and R.C. Krutenat 'Thermal Barrier Coating for Nickel and Cobalt Base Superalloys,' U.S. Patent 4,248,940, February 3, 1981.

[34]M. Koizumi and Y. Tada, 'Establishment of the Functionally Gradient Materials Forum and its Role,' Metals Technology 58 (4) pp. 2-8, (1988).

[35]I. Shiota, 'Fundamental Research on Functionally Gradient Materials,' Proc. of the Conference on Critical Issues in the Development of High Temperature Structural Materials, Warrendale, PA: The Minerals, Metals, and Materials Society. pp. 303-318, (1993).

[36]Y. Itoh and H. Kashiwaya, J. Ceramic Society of Japan100, pp. 476-481, (1992).

[37]T. Hashida, H. Takahashi, and K. Miyawaki, J. Japan Society of Powder and Powder Metallurgy 37, pp. 307-312, (1990).

[38]L.S. Wen, K. Guan, S. W. Qian, C. -F. Lin, and L. S. Fu, 'Ceramic Thermal Barrier Coating for Adiabatic Diesel Engine,' Academia Sinica Materials Protection 25, pp. 14-17, (1992).

[39]W. Lih, E. Chang, C. H. Chao, and M. L. Tsai, Oxidation of Metals 38, pp. 99-124 (1992).

[40]W.J. Brindley and R.A. Miller, 'Thermal Barrier Coating Evaluation Needs,' Conf. on Nondestructive Evaluation of Modern Ceramics, Columbus, Ohio (1992).

[41]T. Hirano, T. Yamada, J. Teraki, M. Niino, and A. Kumakawa, 'A Study on a Functionally Gradient Material Design System for a Thrust Chamber,' Proc. 16th Intl. Symposium on Space and Technology and Science, Sapporo, Japan (1988).

[42]M. Yamanouchi, M. Koizume, T. Hirai and I. Shita, ed., FGM-90, Proc. of the 1st Intl. Sym. on Functionally Gradient Materials, FGM Forum, Sendai, Japan (1990).

[43]J. Holt, M. Koizumi, T. Hirai and Z. Munir, ed., Functionally Gradient Materials, Ceramic Transactions, Proc. of the 2nd Intl. Sym. on Functionally Gradient Materials, presented at the 3rd Int. Ceramic Science and Technology Congress, San Francisco, CA, Vol. 34 (1992).

[44]A. Kawasaki and R. Matanabe, 'Fabrication of Sintered Functioanally Gradient Material by Powder Spray Forming Process,' FGM-90, Yamanouchi et al., ed., Sendai, Japan, pp. 197-202, (1990).

[45]R.L. Williamson and B.H. Rabin, 'Numerical Modeling of Residual Stress in Ni-Al2O3 Gradient Materials,' Ceramic Transactions, Holt et al., ed., Proc. 2nd Intl. Sym. on Functionally Gradient Materials, presented at the 3rd Intl. Ceramic Science and Technology Congress, San Francisco, CA, Vol. 34 (1992).

[46]F. Erdogan and Y.F. Chen, 'Interfacial Cracking of FGM/Metal Bonds,' Ceramic Transactions, Holt et al., ed., Proc. 2nd Intl. Sym. on Functionally Gradient Materials, presented at the 3rd Intl. Ceramic Science and Technology Congress, San Francisco, CA, Vol. 34 (1992).

[47]F. Erdogan, A.C. Kaya, and P.F. Joseph, 'The Crack Problem in Bonded Nonhomogeneous Materials,' J. of Applied Mechanics 58, p. 410-418, (1991).

[48]D.P. Miller, J.J. Lannutti, R.N. Yancey, 'Functionally Gradient NiAl/Al2O3 Structures,' Proc. 16th Annual Conference on Composites and Advanced Ceramic Materials (1992).

[49]J.J. Lannutti, 'Functionally Graded Materials: Properties, Potential and Design Guidelines,' Composites Engineering 4 (1), pp. 81-94 (1994).

[50]D.P. Miller, J.J. Lannutti, R.D. Noebe, 'Fabrication and Properties of Functionally Graded NiAl/Al2O3 Composites,' Journal of Materials Research 8 (5), pp.2004-2013 (1993).

[51]Y.-D. Lee and F. Erdogan, 'Residual/Thermal Stresses in FGM and Laminated Thermal Barrier Coatings,' Lehigh University Technical Report prepared for AFOSR (1994).

[52]M. Case and K. Kokini, 'Thermal Induced Initiation of Interface Edge Cracks in Multilayer Ceramic Thermal Barrier Coatings, 1993 ASME Winter Annual Meeting, Ceramic Coatings Symposium, New Orleans, Louisiana, MD-Vol. 44, pp.149-162. (1993).

[53]F. Erdogan and B.H. Wu, 'Analysis of FGM Specimens for Fracture Toughness Testing' Ceramic Transactions, Holt et al., ed., Proc. 2nd Intl. Sym. on Functionally Gradient Materials, presented at the 3rd Int. Ceramic Science and Technology Congress, San Francisco, CA, Vol. 34 (1992).

[54]A.E. Giannkopoulos, S. Suresh, M. Finot, and M. Olsson, 'Elastoplastic Analysis of Thermal Cycling: Layered Materials with Compositional Gradients', submitted to Acta Metall. Mater. (1994).

[55]D.P. Miller, J.J. Lannutti, W.O. Soboyejo, R.D. Noebe, 'Properties of Functionally Graded NiAl/Al2O3 Composites,' Proc. Intl Symp. on Structural Intermetallics, Champion, PA, Minerals, Metals and Materials Society, Warrendale, PA., pp. 783-790 (1993).

[56]DOE Final Report

[57]Boris Movchan and George Marinsky, ICEBT-Kiev, private communication, 1997.

[58] L.V. Azaroff, "Elements of X-ray Crystallography,"Mcgraw-Hill, New York, 1968.

[59] H. Wang, R. B. Dinwiddie and P. S. Gaal, "Multiple station Thermal Diffusivity Instrument," p. 119-125, Thermal conductivity 23, Thermal Conductivity 23, Ed. by K. E. Wilkes and R. Dinwiddie, Technomic, Lancaster, PA, 1996.

[60]M.P. Borom, C.A. Johnson, and J.A. Ruud, 'TEPCO Phase 1 Task 1.1 Final Report,' GE-CRD Report, (1994)

[61]J.P. McKelvey, Solid State Physics, Malabar, Florida,Krieger Publishing Co., pp. 255-263 (1993).

[62]C. Kittel, Introduction to Solid State Physics, 2nd ed., New York, John Wiley and Sons, p. 139 (1953).

[63]W.D. Kingery, H.K. Bowen, and D.R. Uhlmann, Introduction to Ceramics, 2nd ed. New York, John Wiley and Sons, p. 617 (1976).

[64]W.E. Kuhn, 'Consolidation of Ultrafine Particles,' Ultrafine Particles, W.E. Kuhn, ed., New York, John Wiley and Sons, pp. 41-103 (1963).

[65]W.D. Kingery, 'The Thermal Conductivity of Ceramic Dielectrics,' Progress in Ceramic Science 2, J.E. Burke, ed., New York, Pergamon Press, pp.182-205 (1962).

[66]D-J. Chen and M.J. Mayo, 'Densification and Grain Growth of Ultrafine 3 mol% Y2O3 - ZrO2 Ceramics,' Journal of Nanostructured Materials 2. pp. 469-478, (1993).

[67]M.J. Mayo, 'Synthesis and Applications of Nanocrystalline Ceramics,' Materials and Design 14, pp. 323-329 (1993).

[68]A.J.A. Winnubst, G.S.A.M. Thennissen and A.J. Burggraaf, 'Compaction and Sintering Behaviour of Nano-Crystalline Y-TZP,' Euro Ceramics 1, Proc. 1st Eur. Ceram. Soc. Conf., G. de With, R.A. Terpstra and R. Metselaar, ed., Amsterdam, The Netherlands, Elsevier Applied Science, pp. 1.391-1.397 (1989).

[69]H. Gleiter, 'Nanometer-Sized Microstructures,' Clusters and Cluster-Assembled Materials (Mater. Res. Soc. Symp. Proc. 206), R.S. Averback, D.L. Nelson, and J. Bernholc, ed., Pittsburgh, PA, MRS, pp. 463-473 (1991).

[70]R. Birringer, H. Gleiter, H.-P. Klein, and P. Marquardt, 'Nanocrystalline Materials: An Approach to a Novel Solid Structure with Gas-Like Disorder?' Phys. Lett. 102A, 365-9 (June 1984).

[71]F.R. Charvat and W.D. Kingery, J. Am. Ceram. Soc. 40, 306-315 (September 1957).

[72]E.Y. Litovsky and M. Shapiro, 'Gas Pressure and Temperature Dependences of Thermal Conductivity of Porous Ceramic Materials: Part 1, Refractories and Ceramics with Porosity below 30%,' J. Am. Ceram. Soc. 75, 3425-3439 (1992).

[73]Da-Jiang Chen, 'Densification and Microstructural Evolution in Nanocrystalline Yttria-Stabilized Zirconia Ceramics,' M.S. Thesis, The Pennsylvania State University, 1994.

[74]Y.S. Touloukian, P.E. Liley, S.C. Saxena, Thermal Conductivity, Nonmetallic Liquids and Gases, Vol. 1,2,12,13; IFI/Plenum, New York and Washington (1970).

[75Phase Diagrams for Ceramists-Vol VI, R.S. Roth, J.R. Dennis, and H.F. McMurdie, ed., The Am Ceramic Soc, Westerville, Ohio, 1986, pp. 72-73.

[76]M.R. Jackson and P.A. Siemers, 'Plasma Deposited Ni-Al-Mo Metal-Metal Composite,' MRS Proceedings of Symposium on Plasma Technology Vol. 98, Anaheim, CA, 1987, pp. 347-352.

[77]A.M. Ritter, M.R. Jackson and R.N. Wright, 'Fracture of Steel/Carbide Particulate Composites,' Advances in Fracture Research, K.Salama, K. Ravi-Chandar, D.M.R. Taplin and P. Rama Rao, ed., Pergamon Press, pp.2997-3004, 1989.

[78]A.M. Ritter, M.R. Jackson and R.N. Wright, 'Plasma-Sprayed Stainless Steel/Carbide Particulate Composites,' Processing and Properties for Powder Metallurgy Composites, P. Kumar, K. Vedula and A. Ritter, ed., TMS, Warrendale, PA, pp.59-77, 1988.

[79]M.R. Jackson, P.A. Siemers, J.R. Rairden, R.L. Mehan and A.M. Ritter, 'Composite Structures Produced by Low Pressure Plasma Deposition,' Processing and Properties for Powder Metallurgy Composites, P. Kumar, K. Vedula and A. Ritter, ed., TMS, Warrendale, PA, 1988.

[80]T.E. Strangman, Thin Solid Films, vol 127, pp. 93-105(1985).

[81]A.C. Kaya, H.G. deLorenzi, and K.P. Chow, 'TBC Failure and Life Prediction: Review of Methodology and Parametric Studies,' GE-CRD Technical Report, TEPCO-TBC Program, Phase1-Task 1.2, (1994).

[82]H.F. Nied and A.C. Kaya, 'FRAC2D-Finite Element Based Software for 2-D and Axisymmetric Fracture Analysis,' GE-Technical Report 92CRD-28, (1992).

[83]A.C. Kaya and H.F. Nied, 'Interface Fracture Analysis of Bonded Ceramic Layers Using Enriched Finite Elements,' 1993 ASME Winter Annual Meeting, Ceramic Coatings Symposium, MD-Vol. 44, (1993).

[84]Muhsin Ciftcioglu and Merrilea J. Mayo, 'Processing of Nanocrystalline Ceramics,' Superplasticity in Metals, Ceramics, and Intermetallics (Mater. Res. Soc. Symp. Proc. 196), M.J. Mayo, M. Kobayashi, and J. Wadsworth, ed. Pittsburgh, PA: MRS, 1990. pp. 77-92.

[85]J.R. Seidensticker, M.J. Mayo, and K. Osseo-Assare, 'Adsorption as a Method of Doping 3 Mol% Yttria Stabilized Zirconia Powder with Copper Oxide,' J. Am. Ceram. Soc. 76, pp. 1844-8, (1993).

[86]M.J. Mayo, D-J. Chen, M. Sharma, and B.A. Cottom, 'Wet Processing of Nanocrystalline Yttria-Stabilized Zirconia,' to be submitted to J. Am. Ceram. Soc.

[87]D.C. Hague and M.J. Mayo, 'Sinter-Forging of Chemically Precipitated Nanocrystalline TiO2,' Mechanical Properties and Deformation Behavior of Materials Having Ultrafine Microstructures, M. Nastasi, D. Parkin, and H. Gleiter, ed., Dordrecht, The Netherlands: Klewer, pp. 539-545, 1993.

[88]B.D. Cullity, Elements of X-Ray Diffraction, Reading, Mass: Addison-Wesley Publishing Co, p. 99, 1956.

[89]V.A. Hackley, M. A. Anderson, and S. Spooner, 'A Small-Angle X-Ray Scattering Study of Microstructure Evolution During Sintering of Sol-Gel-Derived Porous Nanophase Titania,' J. Mater. Res. 9, pp. 2555-71 (1992).

[90] L.M. Clark III and R.E. Taylor, "Radiation Loss in the Flash Method of Thermal Diffusivity," J. App. Phys., **46** [2] 714-719 (1975).

[91] Ralph B. Dinwiddie, Stephen C. Beecher, Wallace D. Porter and Ben A. Nagaraj, "The Effect of Thermal Ageing on the Thermal Conductivity of Plasma Sprayed and EBPVD Thermal Barrier Coatings," ASME-96-GT-282.

[92] R. C. Garvie, "The Thermal Conductivity of Stabilized Zirconia," J. of Mat. Sc., **11** 1365-1367 (1976).

[93] Efim Ya. Litovsky and Michael Shapiro, "Gas Pressures and Temperature Dependences of Thermal Conductivity of Porous Ceramic Materials: Part 1, Refractories and Ceramics with Porosity below 30%," J. Am. Ceram. Soc., **75** [12] 3425-39 (1990).

[94] Y. S. Touloukian and E. H. Buyco, " Specific Heats of Non-Metallic Solids," Thermophysical Properties of Matter-V. 5, Plenum, New York, 1970.

[95] W. N. Lawless and T. K. Gupta, "Thermal properties of tetragonal zirconia at low temperatures," Phys. Rev. B, **28** [10] 5507-5510 1983.

[96] R. P. Ingel and Lewis III, "Lattice Parameters and Density for Y2O3-Stabilized ZrO2," J. Am. Ceram. Soc., **69** [4] 325-332 (1986).

FIGURE CAPTIONS

Figure 1-1. By incorporating high-conductivity low-expansion materials—such as Cr_7C_3—in the FGM, improved thermal system reliability may be achieved while maintaining current temperature profiles in the outermost metallic bond coat region.

Figure 3-1. For current thermal barrier systems, the sharp discontinuity in both thermal expansion and thermal conductivity at the bond coat/TBC interface leads to large interface stresses.

Figure 3-2. For the illustrated two-layer bondcoat with stepwise reduction in thermal expansion (67%metal+33%ceramic followed by 33%metal+67%ceramic), expansion mismatch is partially accommodated over the bond coat thickness. However, the parallel reduction in thermal conductivity through the bond coat leads to an increased metal temperature (T_{3b}) at the TBC interface.

Figure 3-3. Three modes of delamination failure observed in TBC systems: (1) free-edge delamination; (2) buckling failure far from free edges; (3) delamination from transverse cracks. Arrows indicate loadings in the TBC.

Figure 3-4. Multilayer graded coatings used in diesel engine TBCs by (a) Caterpillar and (b) Cummins/UTRC [40].

Figure 4-1. Using a high-conductivity low-expansion component in the region graded with metal, the thermal expansion mismatch is accommodated over the graded thickness without a increased metal temperature in the region adjacent to the insulating ceramic.

Figure 4.2. For FGMs with continuous gradients from the metallic substrate to FGM outer ceramic, the high-conductivity FGM achieves interface temperature comparable to the monolithic metabond coat, while it achieves expansion accommodation comparable to the low-conductivity FGM.

Figure 4-3. Metal carbides and refractory metals have thermal conductivity similar to metal substrate materials, but thermal expansion similar to the insulating ceramic materials [74]. Using different blends of metal, metal carbide, refractory metal, and ceramic, gradients in thermal expansion and thermal conductivity can be uncoupled to control stress distribution throughout the FGM.

Figure 4-4. The ternary phase diagram for Cr-O-Zr [75] and schematic quaternary phase diagram Cr-O-Zr-C indicate an example candidate system for a high-conductivity FGM. High-conductivity low-expansion chromium metal carbides can be isolated from insulating zirconia by using an interlayer of Cr_2O_3.

Figure 5-1. Approximate locations in Ni-Cr-Al-C quaternary space for the candidate alloys. Low-expansion alloys 1-4 contain ~45 volume percent of αCr plus M_7C_3. The microstructure of alloy 2 after equilibration at 1100°C is shown as an example. The large bright phase is M_7C_3, the small bright phase is αCr, the light gray phase is βNiAl, and the dark matrix is γNi solid solution.

Figure 5-2. Estimates used in the stress/temperature model of expansion, thermal conductivity, modulus and specific heat, as functions of temperature, for the bond coat alloys.

Figure 5-3. FGM bond coat case studies were done for a number of materials combinations using the labeling format illustrated.

Figure 5-4. FGM bond coat case studies were carried out for three-layer bond coats of 0.1 mm thickness, with individual layer thicknesses as noted for cases A, B and C.

Figure 5-5. Stress distribution from the substrate through to the TBC surface are illustrated for Case A conditions, for four different outer-bond coat alloys and two different mid-bond coat alloys, all with alloy 7 as the inner bond coat alloy.

Figure 5-6. Thermal expansion behaviormeasured for alloys 1-4, compared to yttria stabilized zirconia.

Figure 5-7. Weight change in cyclicoxidation for alloys 1-4: 50 minutes at 1100°C and 10 minutes for cooling cycle. Microstructure of oxidized alloy 2 after 525 cycles to 1100°C is also illustrated. The outer oxidized surface is out of view at the bottom. The unaltered structure is at the extreme top of the micrograph. Substantial depletion of Al from the structure has eliminated the NiAl phase from the outer regions of the sample. Internal oxidation has led to attack of the Cr-rich phases, both α (shown here) and the carbide (not shown).

Figure 5-8. Vapor pressure/temperature relations for pure elements can be used to estimate alloy evaporation. The binary Al-Si phase diagram is superimposed on the plot, with pure Al at the left and pure Si at the right. As the pool is melted by the 0.5KW electron beam, and then is subjected sequentially to higher beam powers, the pool temperature increases and evaporation begins, with Al evaporating proportionately faster than Si. The initial regions of the deposit are Al-rich, with the remnant pool enriched in Si. At the highest power levels, the pool has been enriched sufficiently in Si so that significant Si is evaporating as the pool is being depleted toward zero volume.

Figure 5-9. Vapor pressure/temperature relations for evaporation of pure Cr, Si, Zr and Al are useful for understanding the measured chemical gradients for binary Al-Cr, Al-Si, and Al-Zr deposition under increasing power shown in Figure 5-8. The substrates are off the plots to the left, so that only the deposit chemistries are shown. The initial deposited material is Al-enriched, with the last regions deposited being rich in the lower-vapor pressure solute element.

Figure 5-10. Evaporation of a complex Al-Cr-Si-Y alloy of fixed source volume results in a similar chemical gradation as did the binary alloys. Even after heat treatment to diquate the coating and react it with the substrate, retention of chemical gradients results in Cr_3Si and α Cr phases in the outer portions of the coating structure.

Figure 5-11. Specific heat capacity of zirconia

Figure 5-12. Thermal conductivity as a function of temperature in nanocrystalline tetragonal zirconia (5.8 wt. % yttria). Densities (% of theoretical) and grain diameters (in nm) are also indicated

Figure 5-13. Comparison of conductivities measured at 100 C in nanocrystalline zirconia (5.8wt% yttria) with those calculated from Equation 5.

Figure 5-14. Effect of yttria content on thermal conductivity. Phases present in the samples are as follows: M=monoclinic, T=tetragonal, C=cubic. Densities (% of theoretical) and grain diameters (in nm) are also shown.

Figure 5-15. Thermal conductivity of pure monoclinic zirconia (98% dense, 63 nm grain diameter) vs 1/T.

Figure 5-16. Comparison of thermal conductivity for nanocrystalline zirconias of the present study (open symbols) with comparable data for commercial zirconia thermal barrier coatings (closed symbols).

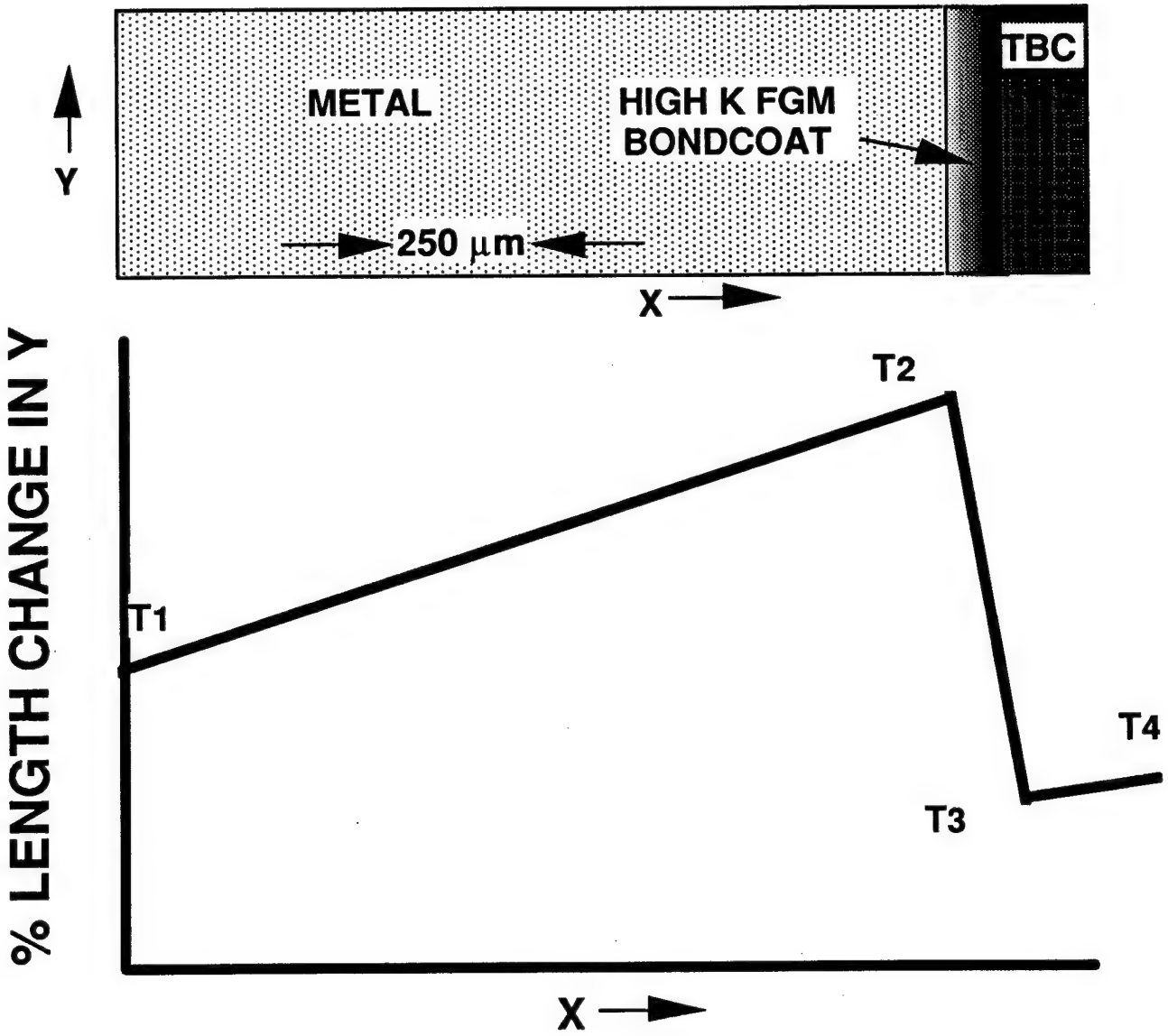
METAL
HIGH K FGM
BONDCOAT
TBC
Y
250 μm
X
% LENGTH CHANGE IN Y
T1
T2
T3
T4
X

Figure 1-1

expansion discontinuity at T3

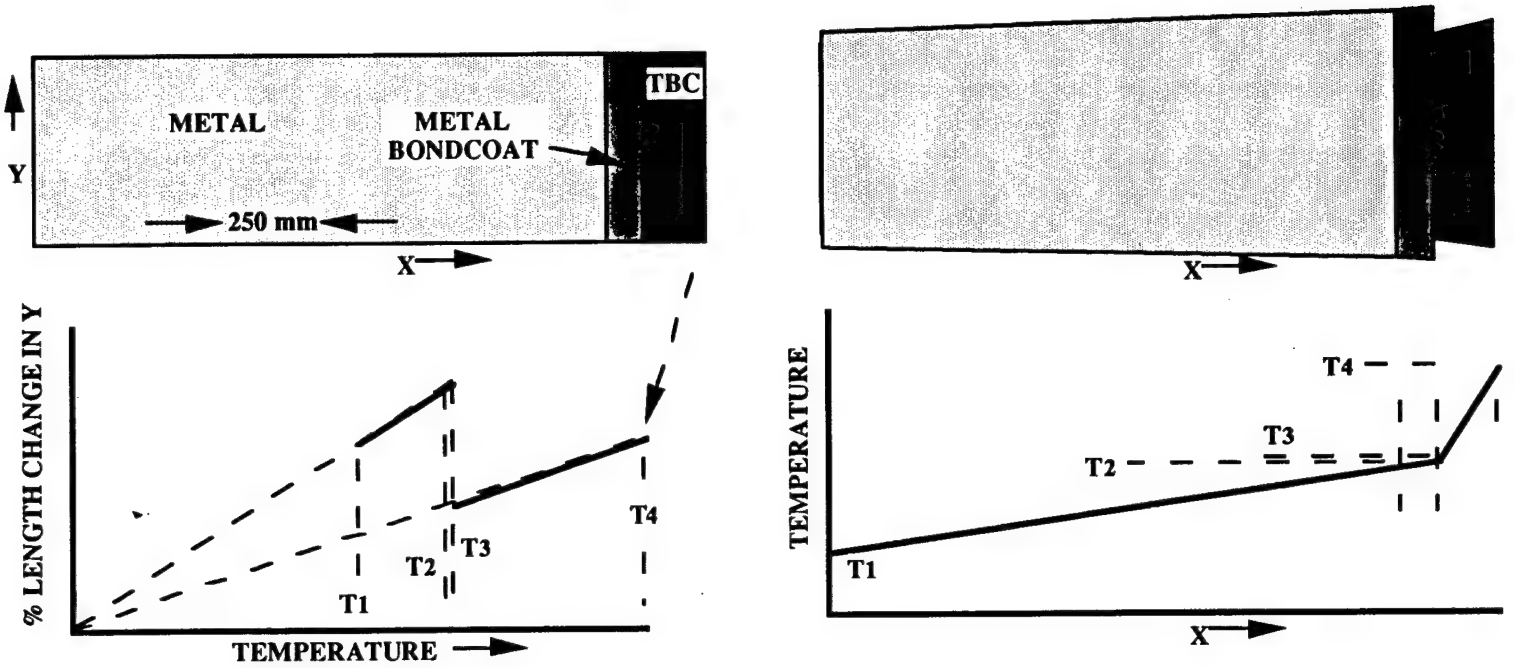

k(metal)=k(bond coat)>>k(thermal barrier)
α(metal)=α(bond coat)>>α(thermal barrier)

Figure 3-1

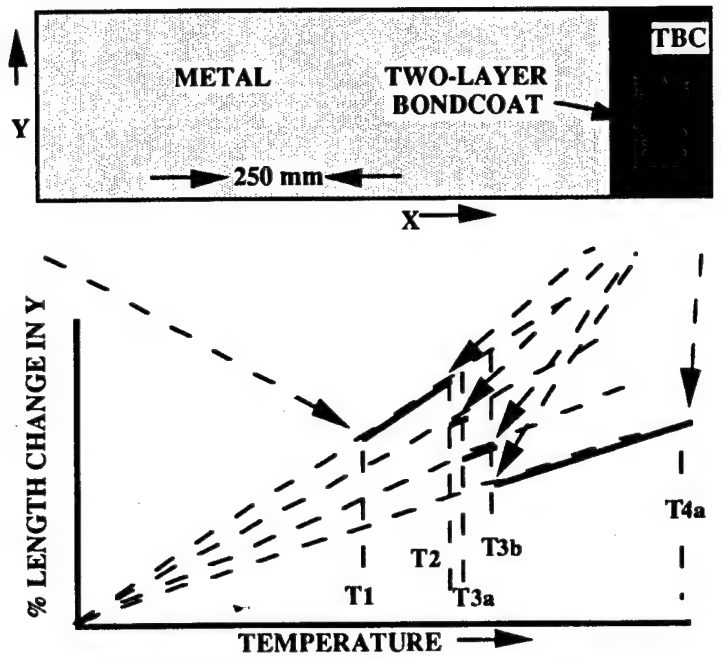

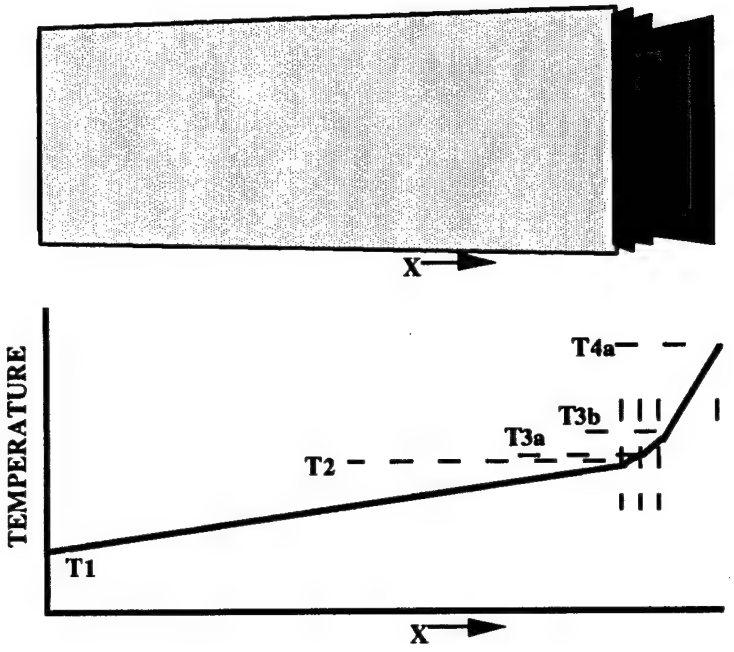

Two layers in bond coat:
67% metal - 33% ceramic
33% metal - 67% ceramic

k(metal)>k(bond coat)>k(thermal barrier)
α(metal)>α(bond coat)>α(thermal barrier)

Figure 3-2

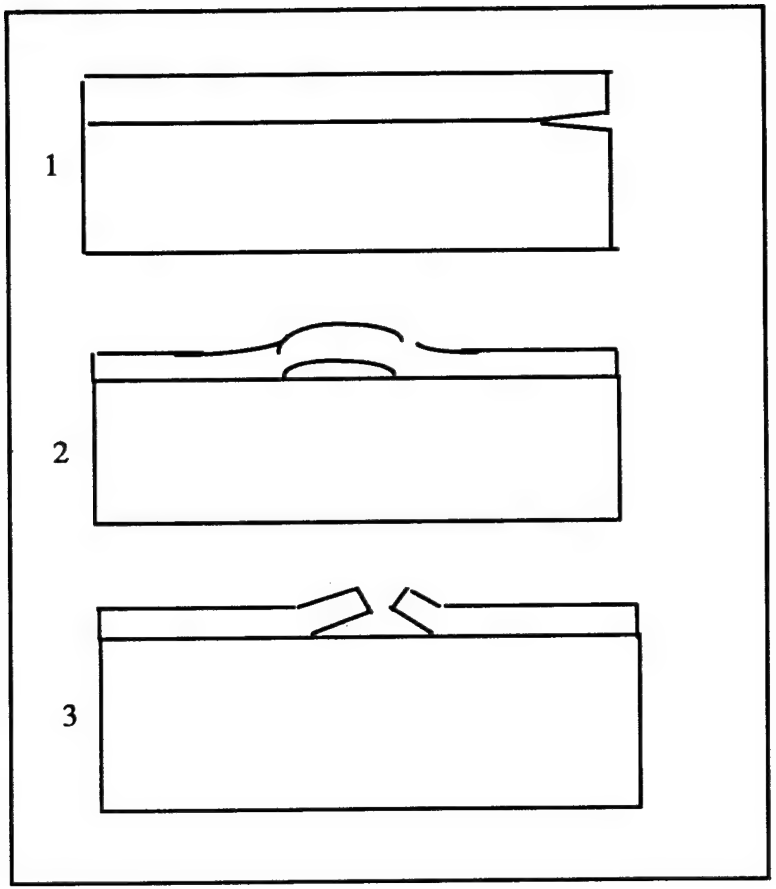

Ahmet Figure 3-3. Three modes of delamination failure have been observed in TBC systems: (1) free-edge delamination; (2) buckling failure far from free edges; (3) delamination from transverse cracks.

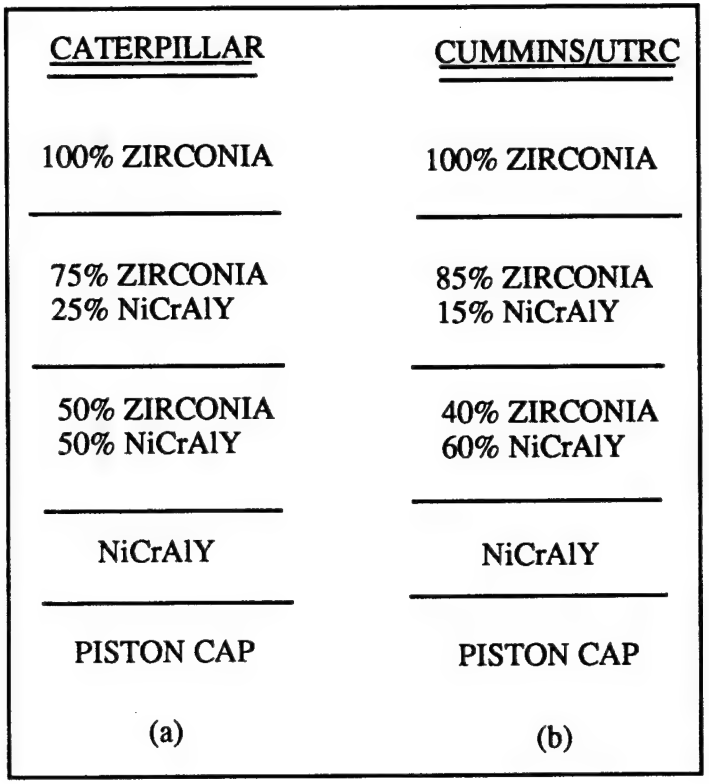
CATERPILLAR
100% ZIRCONIA
75% ZIRCONIA
25% NiCrAlY
50% ZIRCONIA
50% NiCrAlY
NiCrAlY
PISTON CAP
(a)
CUMMINS/UTRC
100% ZIRCONIA
85% ZIRCONIA
15% NiCrAlY
40% ZIRCONIA
60% NiCrAlY
NiCrAlY
PISTON CAP
(b)

Figure 3-4

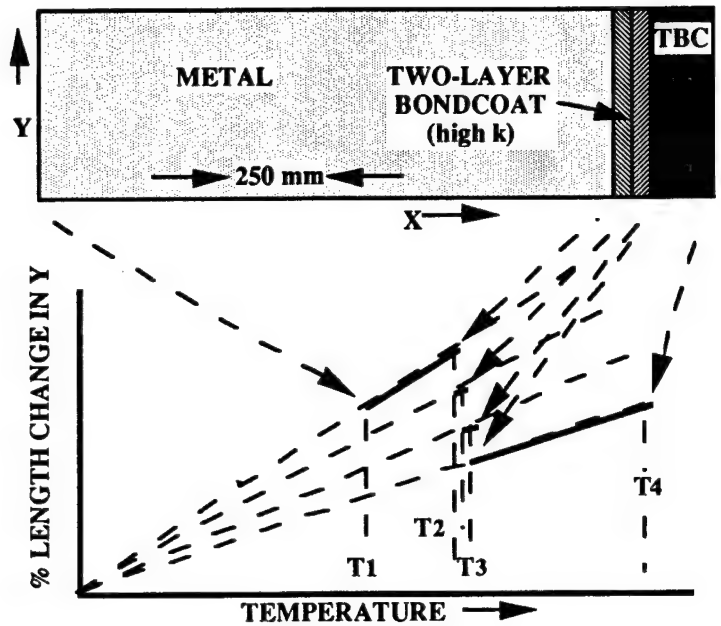

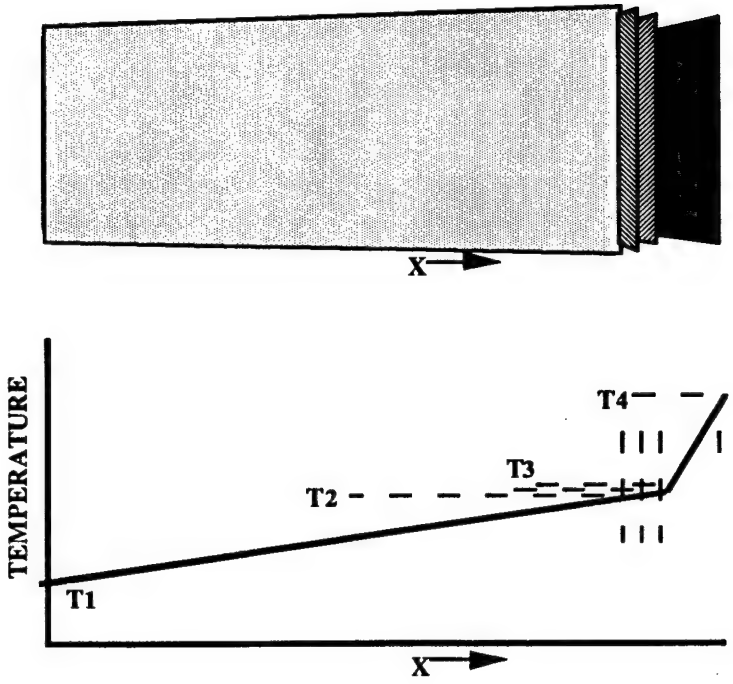

Two layers in bond coat:
67% metal - 33% high k/low α
33% metal - 67% high k/low α

k(metal)=k(bond coat)>>k(thermal barrier)
α(metal)>α(bond coat)>α(thermal barrier)

Figure 4-1

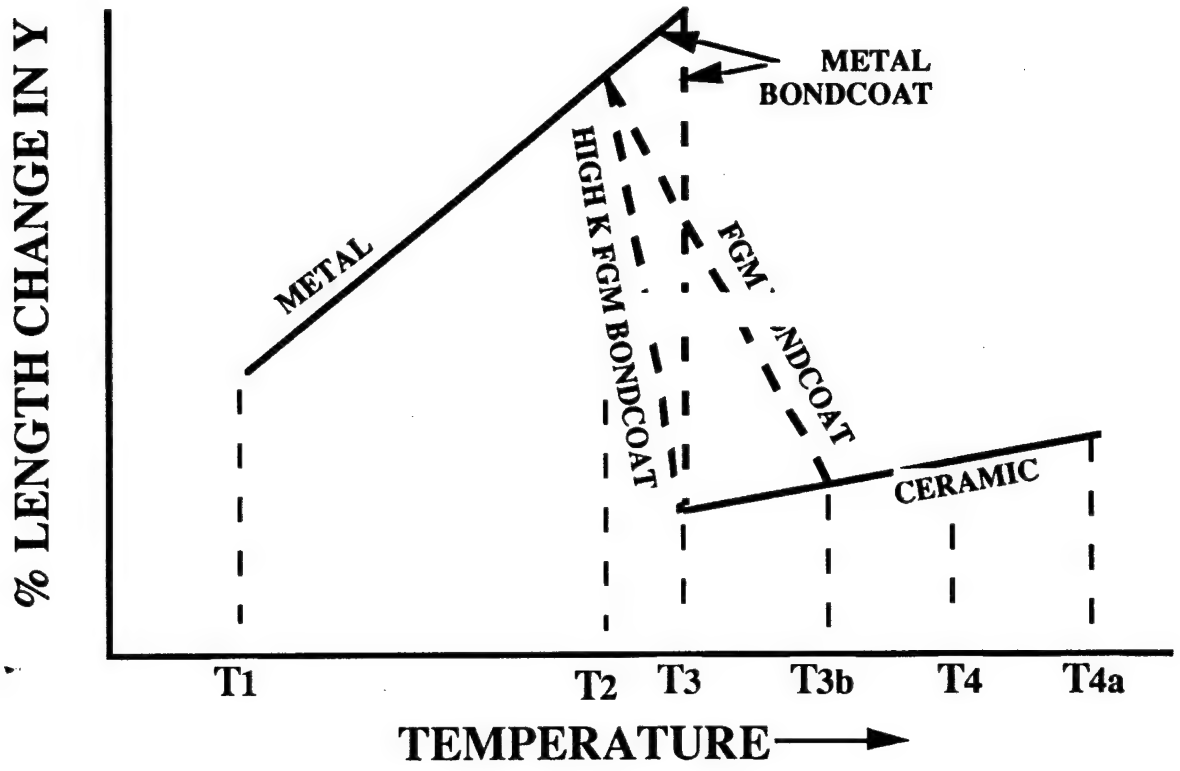
% LENGTH CHANGE IN Y
METAL
METAL BONDCOAT
HIGH K FGM BONDCOAT
FGM
NDCOAT
CERAMIC
T1
T2
T3
T3b
T4
T4a
TEMPERATURE

Figure 4-2

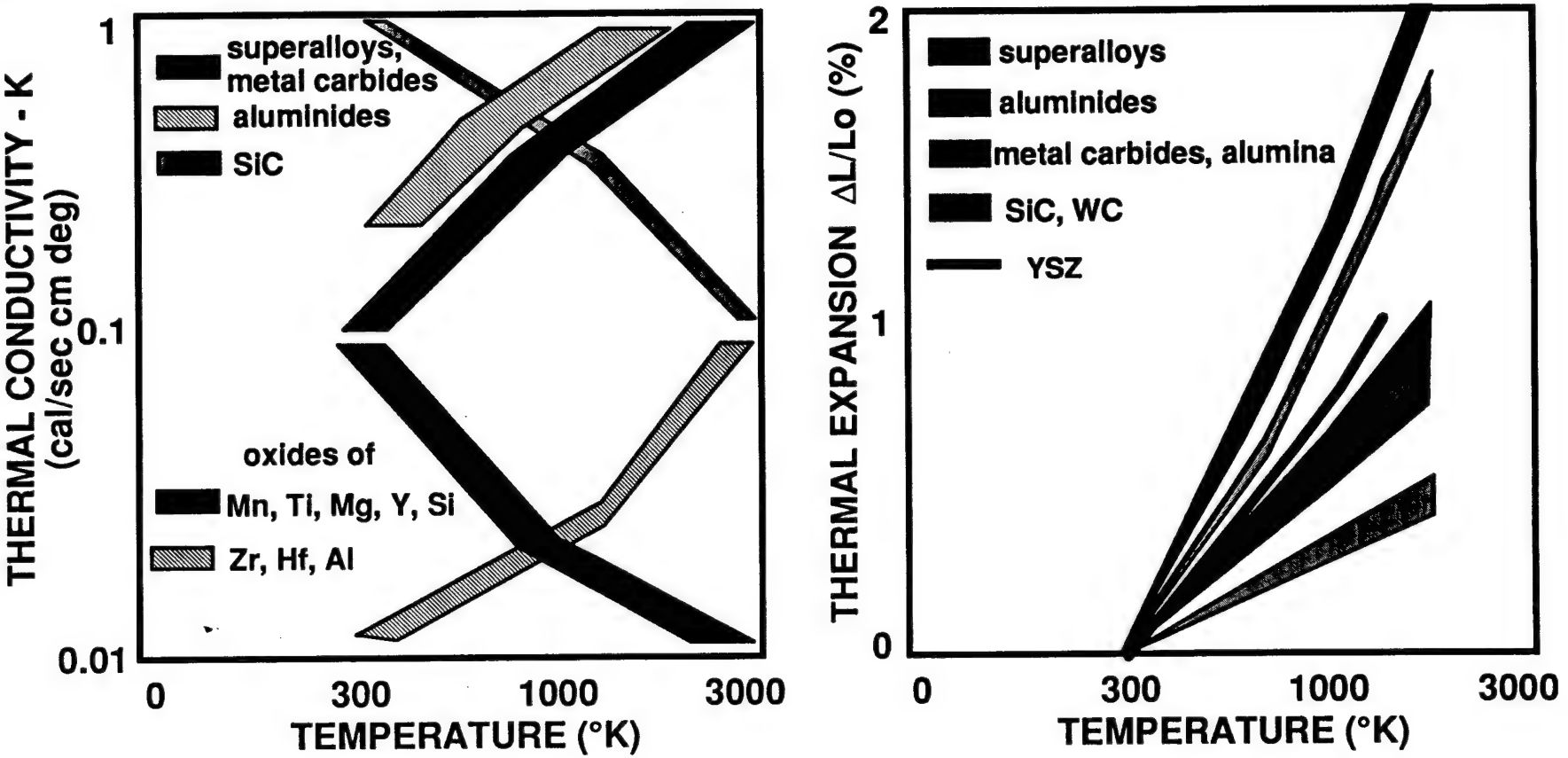
THERMAL CONDUCTIVITY - K
(cal/sec cm deg)
1
0.1
0.01
superalloys,
metal carbides
aluminides
SiC
oxides of
Mn, Ti, Mg, Y, Si
Zr, Hf, Al
0
300
1000
3000
TEMPERATURE (°K)
THERMAL EXPANSION ΔL/Lo (%)
2
1
0
superalloys
aluminides
metal carbides, alumina
SiC, WC
YSZ
0
300
1000
3000
TEMPERATURE (°K)

Figure 4-3

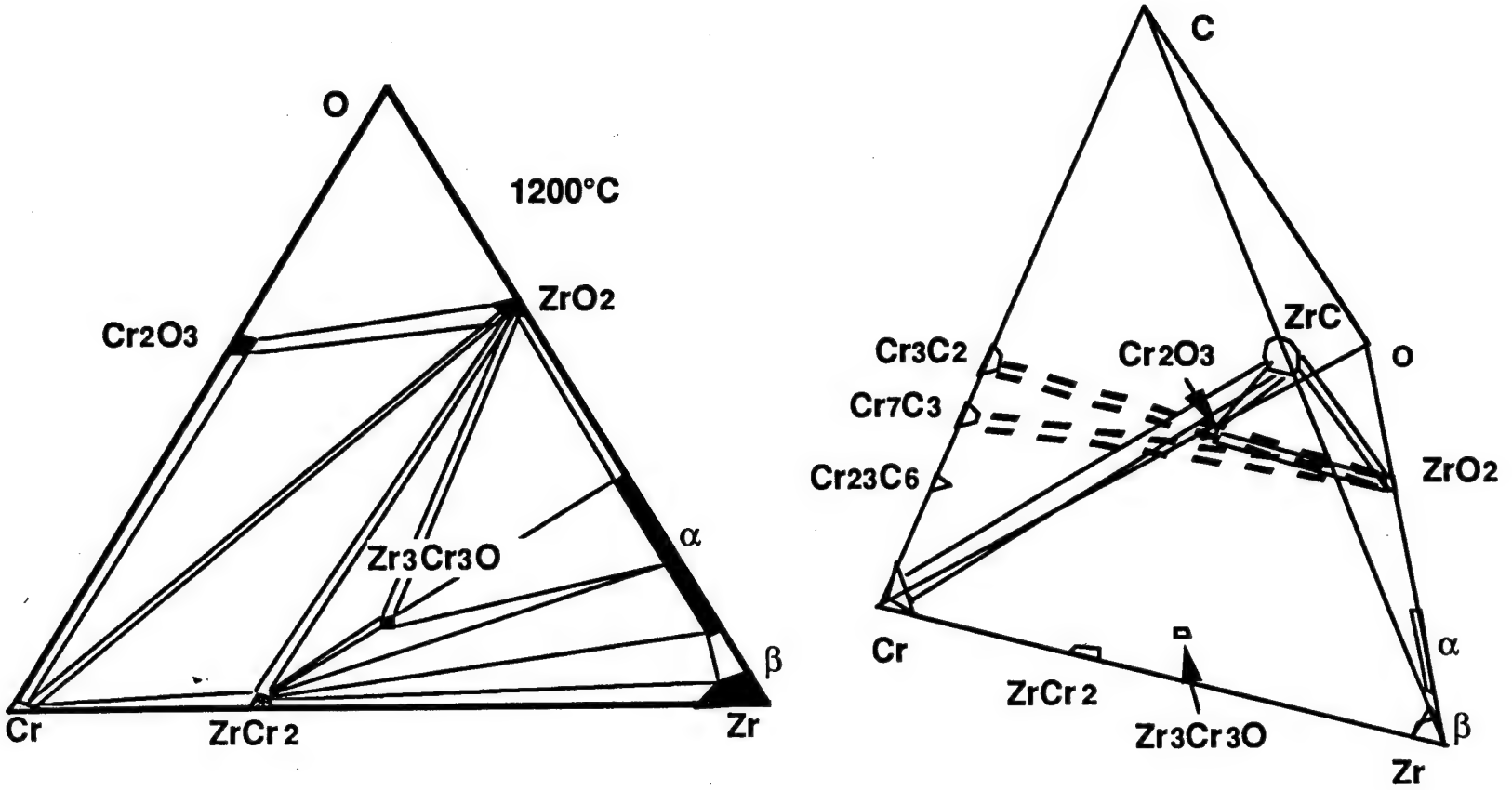
O
1200°C
ZrO2
Cr2O3
Zr3Cr3O
α
β
Cr
ZrCr2
Zr
C
ZrC
Cr3C2
Cr2O3
O
Cr7C3
Cr23C6
ZrO2
Cr
α
ZrCr2
Zr3Cr3O
β
Zr

Figure 4-4

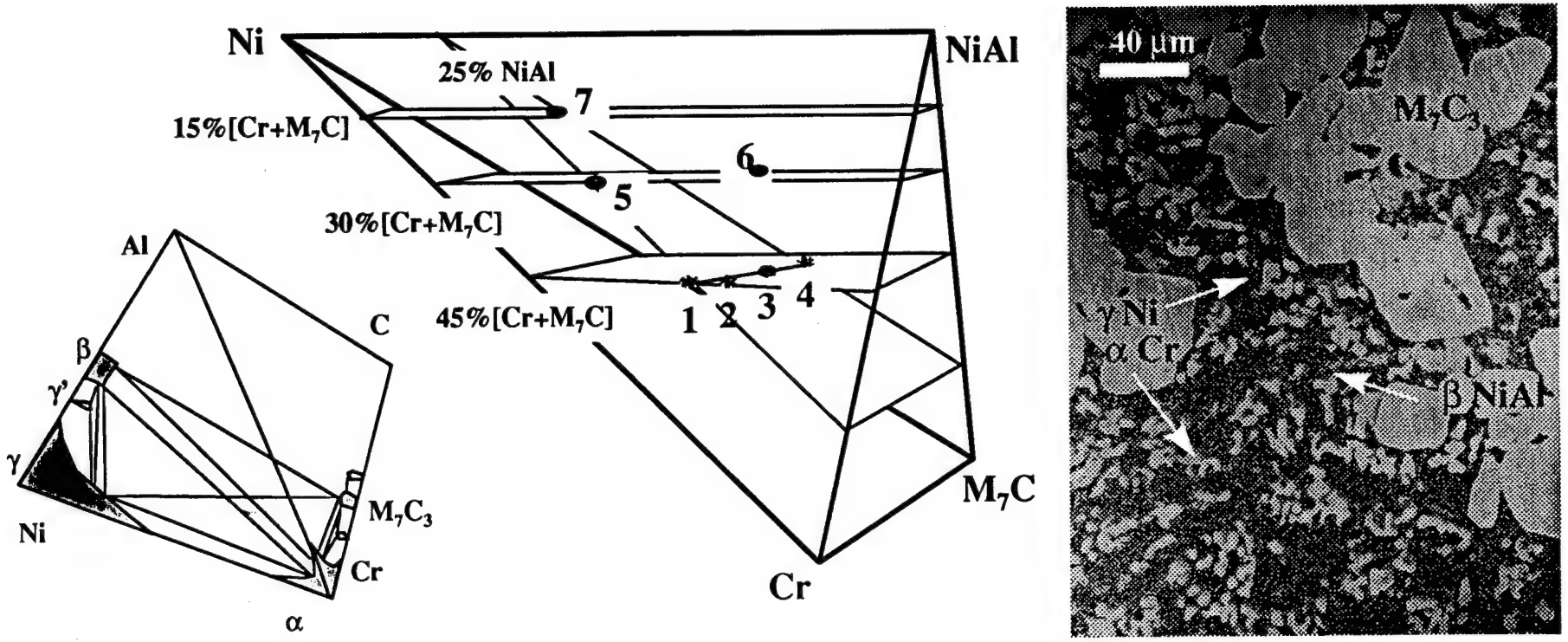
Ni
25% NiAl
NiAl
15%[Cr+M7C]
7
6
5
30%[Cr+M7C]
45%[Cr+M7C]
1
2
3
4
Al
C
β
γ'
γ
Ni
M7C3
Cr
α
M7C
Cr
40 μm
M7C3
γ Ni
α Cr
β NiAl

Figure 5-1

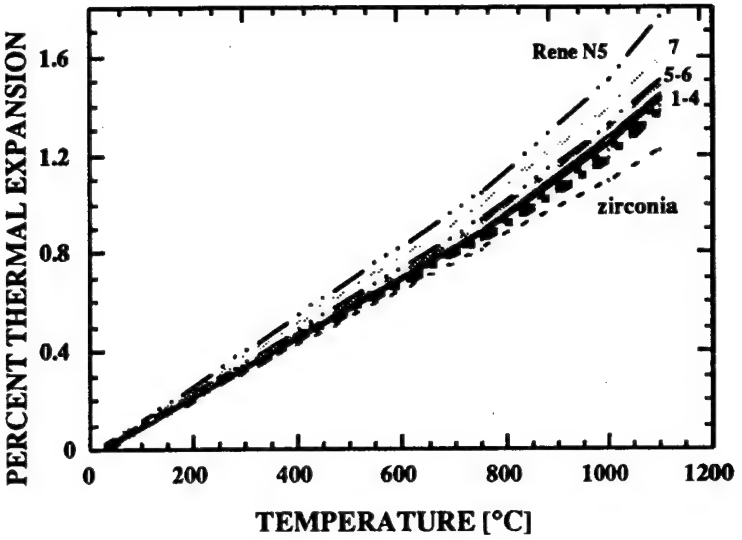
PERCENT THERMAL EXPANSION
TEMPERATURE [°C]
Rene N5
7
5-6
1-4
zirconia
0
0.4
0.8
1.2
1.6
0
200
400
600
800
1000
1200

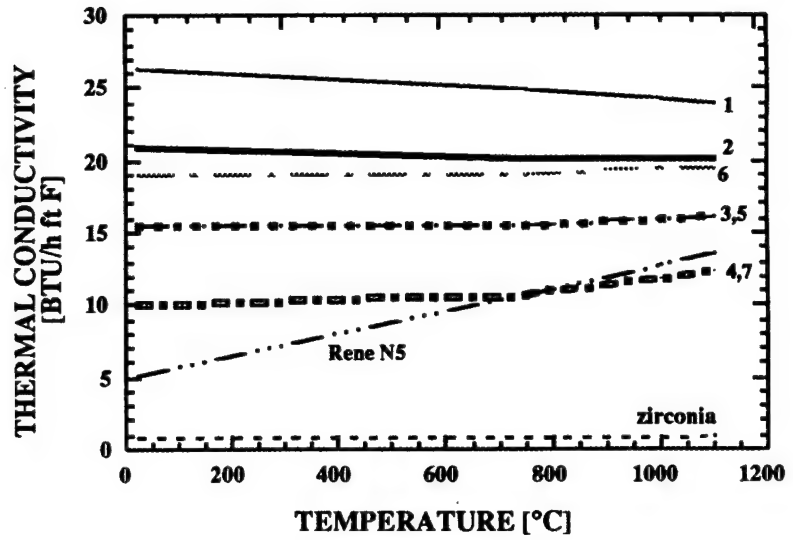
THERMAL CONDUCTIVITY [BTU/h ft F]
TEMPERATURE [°C]
1
2
6
3,5
4,7
Rene N5
zirconia
0
5
10
15
20
25
30
0
200
400
600
800
1000
1200

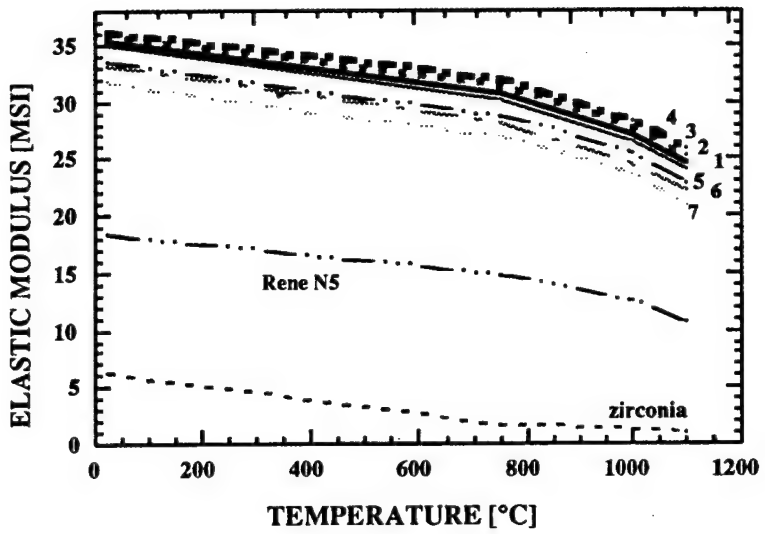
ELASTIC MODULUS [MSI]
TEMPERATURE [°C]
4
3
2
1
5
6
7
Rene N5
zirconia
0
5
10
15
20
25
30
35
0
200
400
600
800
1000
1200

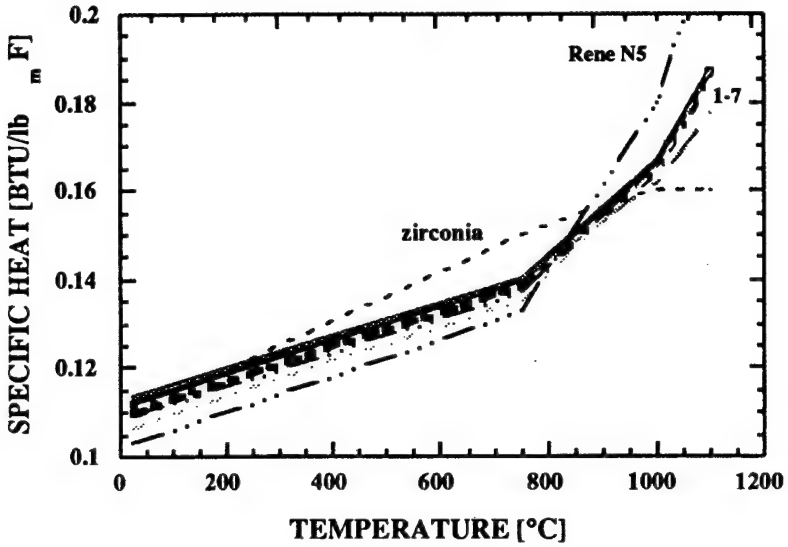
SPECIFIC HEAT [BTU/lb F]
TEMPERATURE [°C]
Rene N5
1-7
zirconia
0.1
0.12
0.14
0.16
0.18
0.2
0
200
400
600
800
1000
1200

Figure 5-2

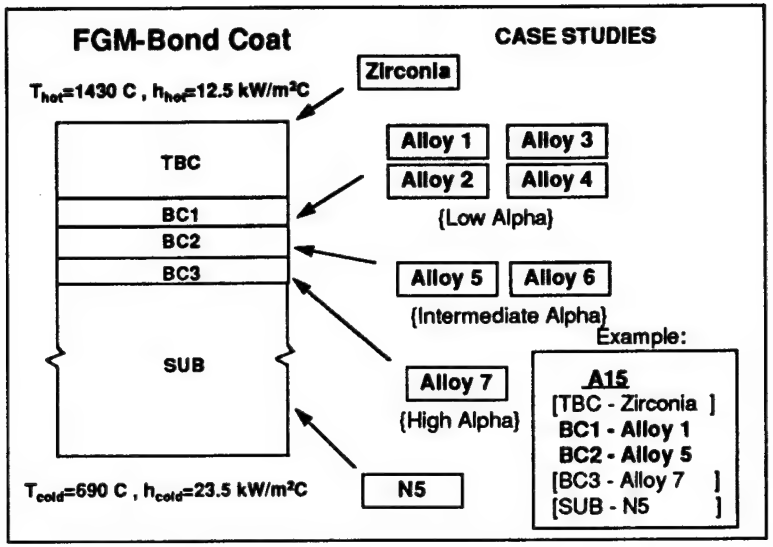

Figure 5.3. FGM Bond Coat Case Studies - Material Combinations

Figure 5-3

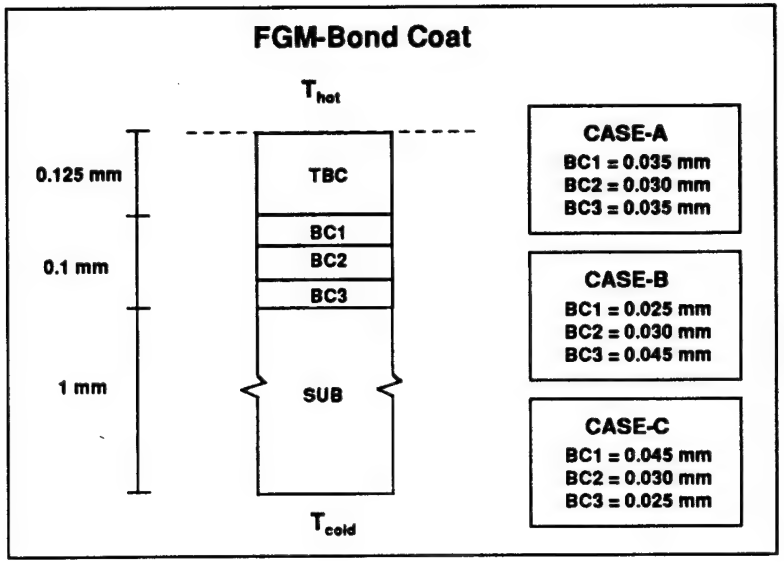

Figure 5.4. FGM Bond Coat Case Studies - Layer Thicknesses

Figure 5-4

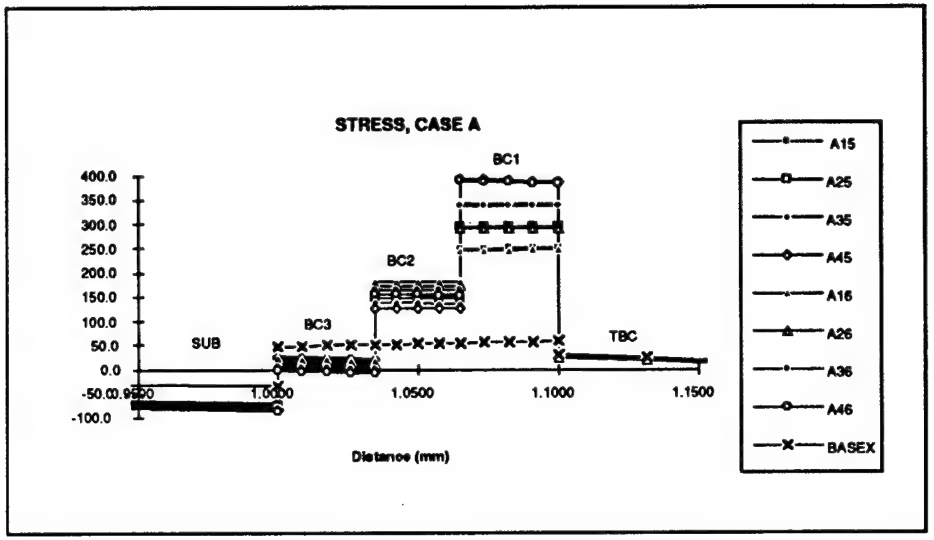

Figure 5.5. Stress Distribution for FGM Bond Coat - Case A

Figure 5-5

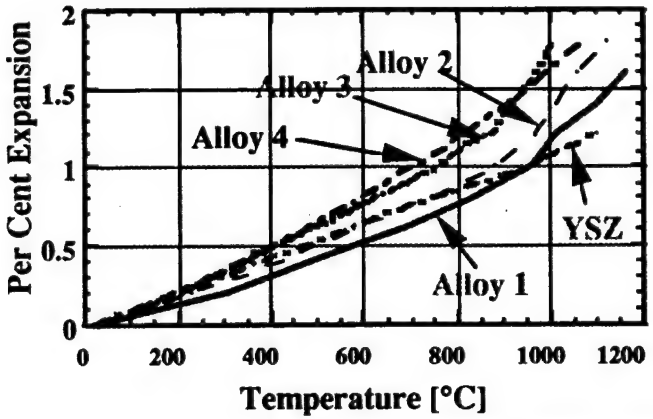

Figure 5-6

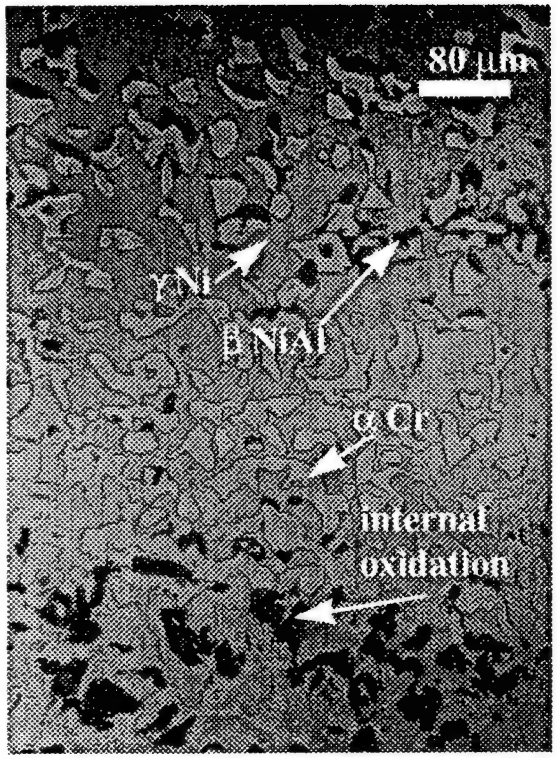

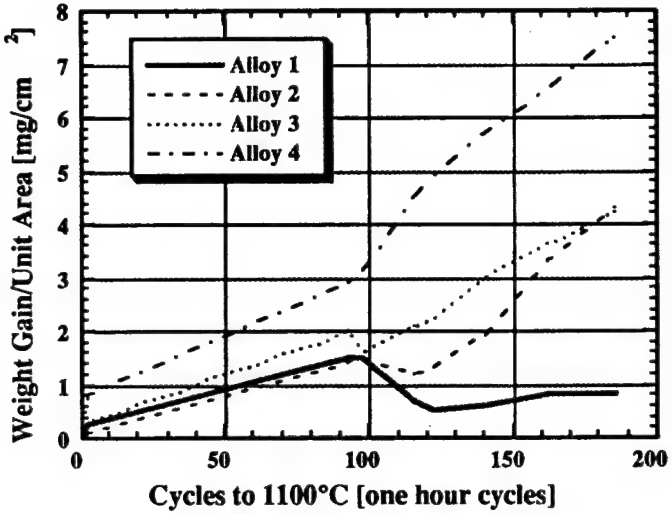

Figure 5-7

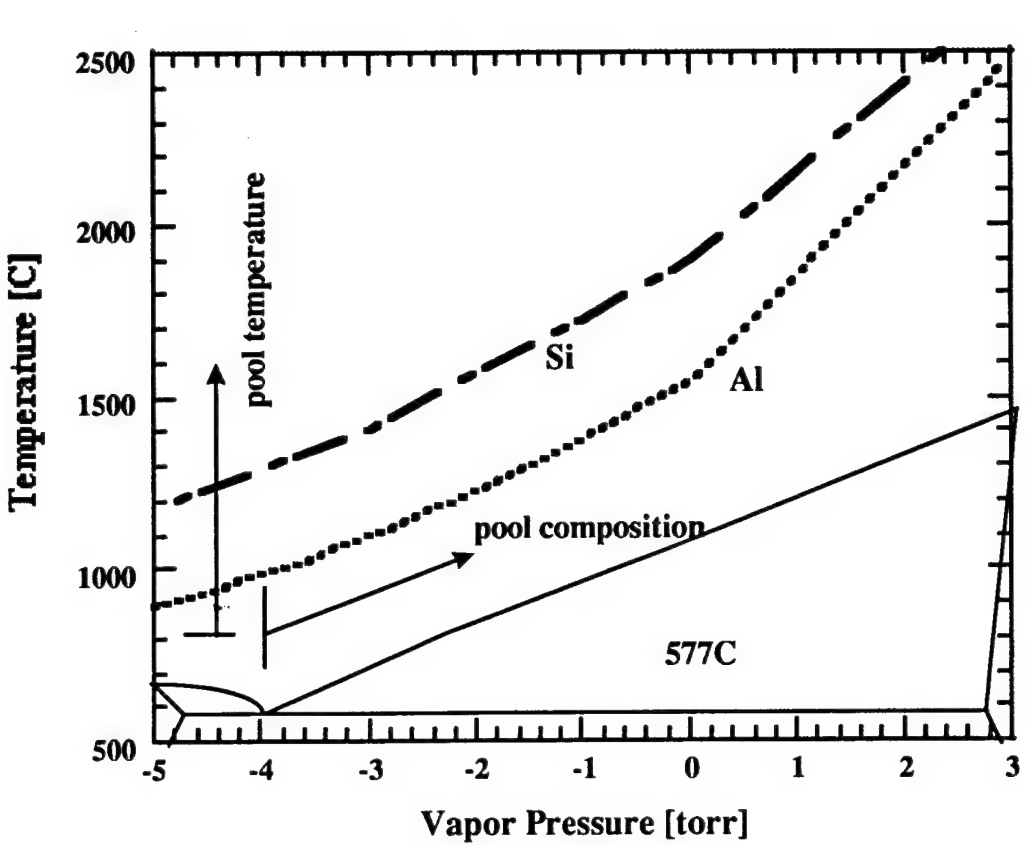
2500
2000
1500
1000
500
Temperature [C]
pool temperature
Si
Al
pool composition
577C
-5
-4
-3
-2
-1
0
1
2
3
Vapor Pressure [torr]

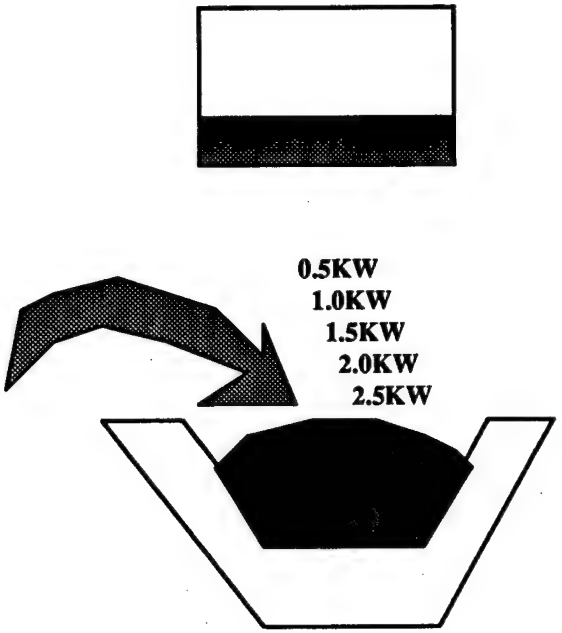
0.5KW
1.0KW
1.5KW
2.0KW
2.5KW

Figure 5-8

Temperature [C]
2500
2000
1500
1000
500
Zr
Si
Cr
Al
-5
-4
-3
-2
-1
0
1
2
3
Vapor Pressure [torr]
Atomic Per Cent
100
10
1
0.1
0.01
Al-Cr
Al-Si
Al-Zr
Cr
Si
Zr
0
5
10
15
20
25
Approximate Distance [microns]

Figure 5-9

Figure 5-10

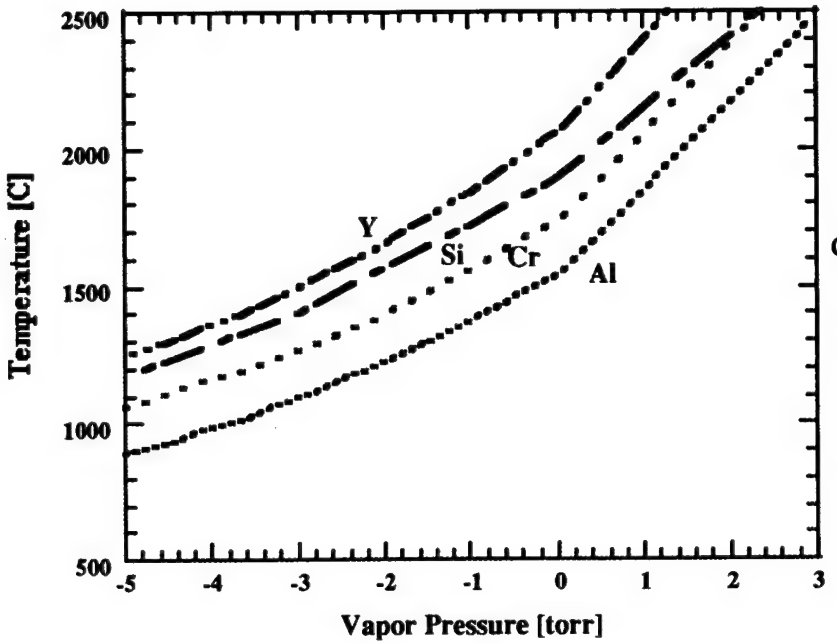

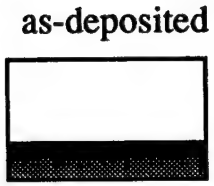

deposit at low temperature
+ heat treat
-> alloyed NiAl coating

growth by
reaction in heat
treatment

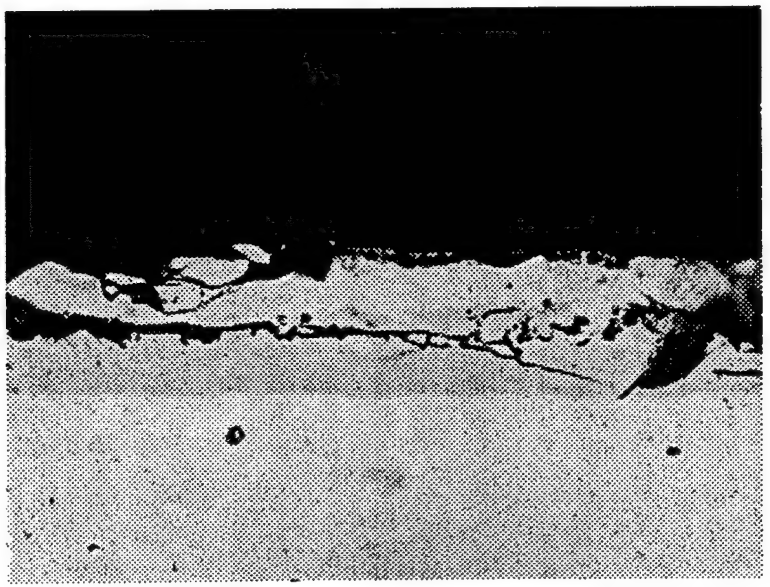

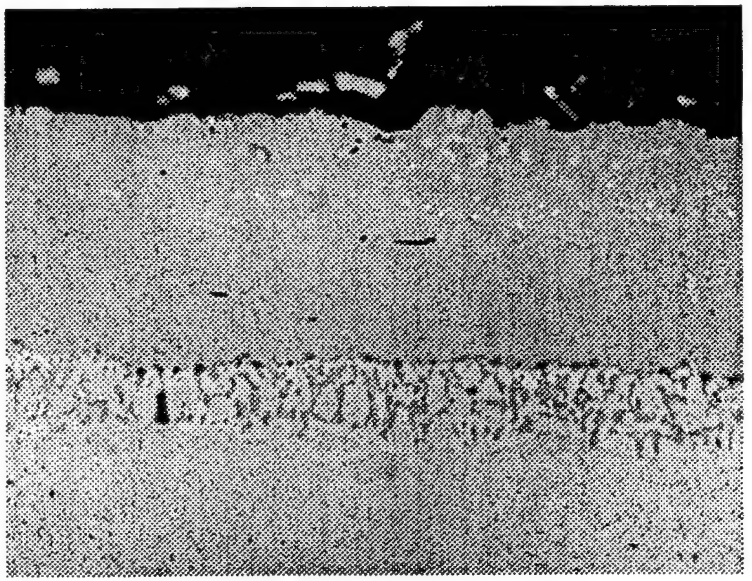

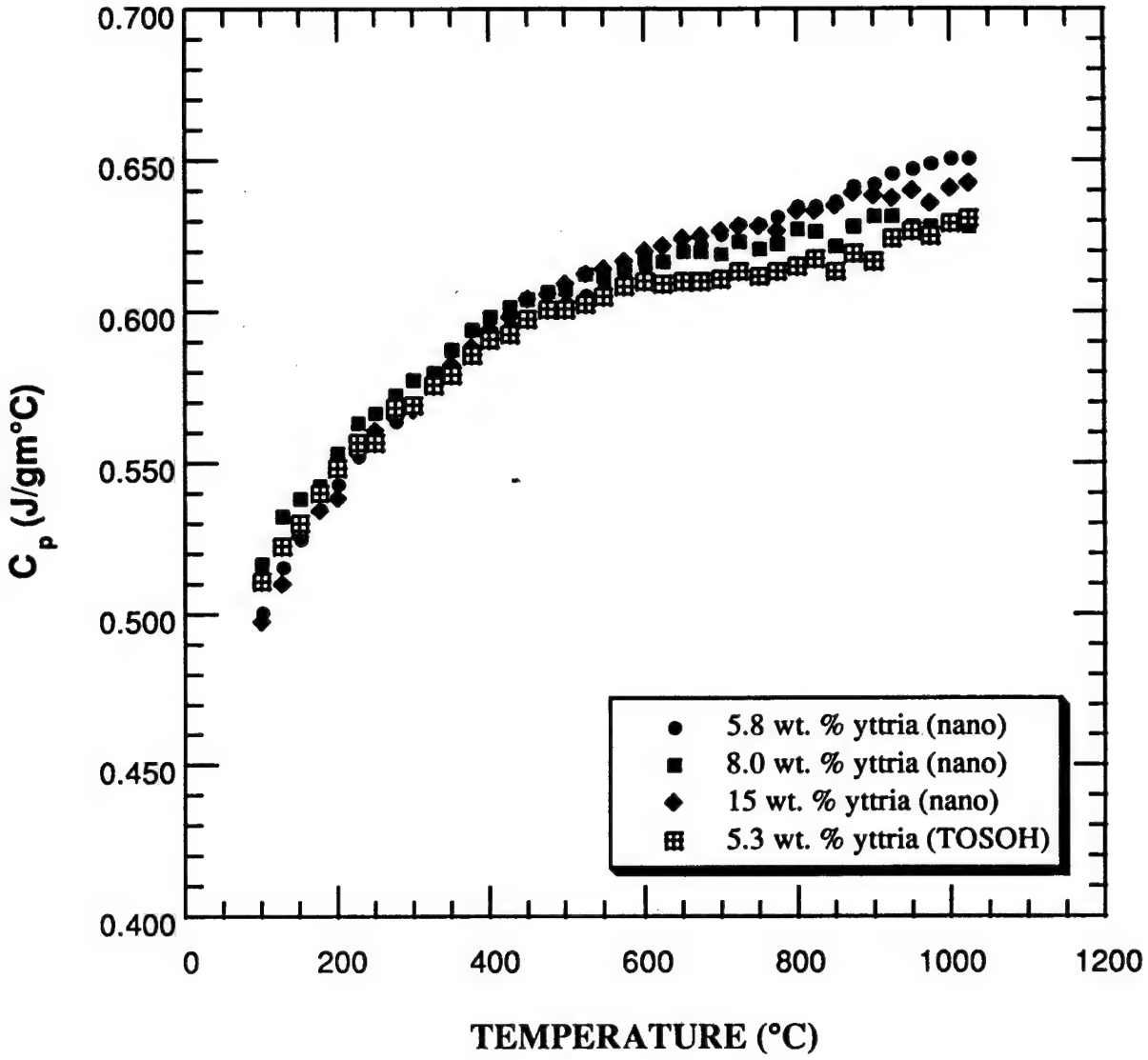

Figure5.11. Specific heat capacity of zirconia

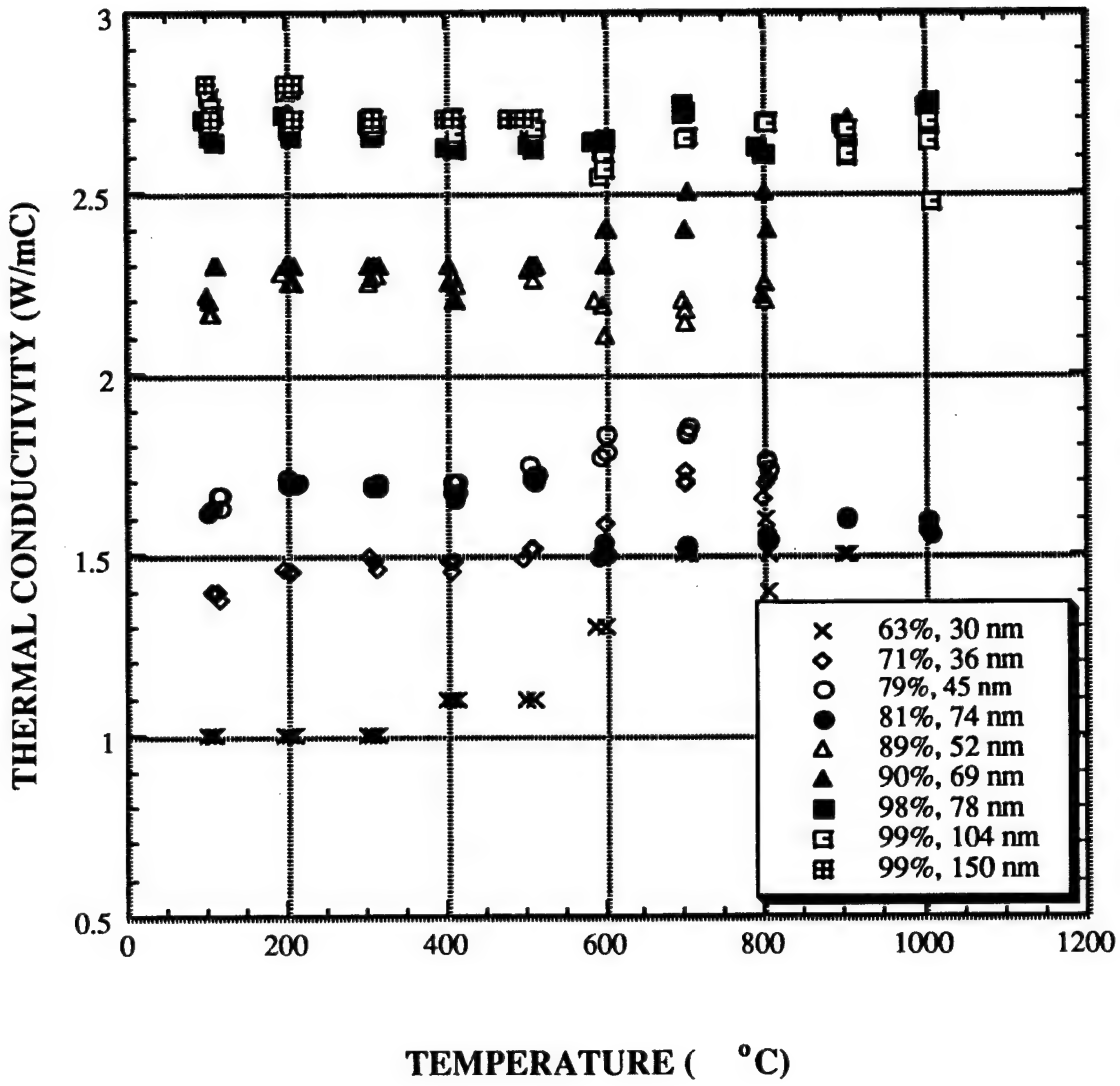

Figure 5.12. Thermal conductivity as a function of temperature in nanocrystalline tetragonal zirconia (5.8 wt. % yttria). Densities (% of theoretical) and grain diameters (in nm) are also indicated

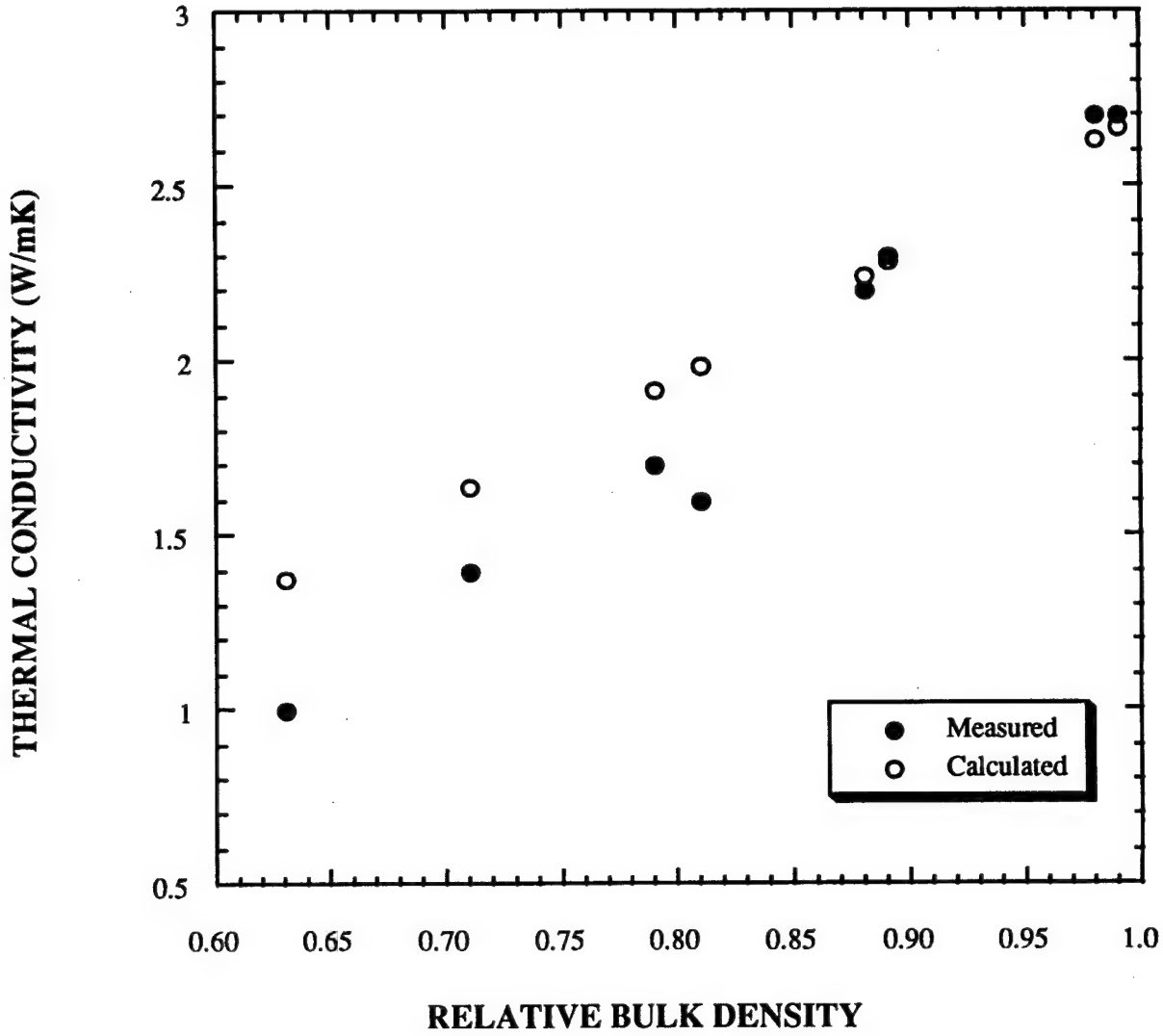

Figure 5.13. Comparison of conductivities measured at 100 °C in nanocrystalline zirconia (5.8wt% yttria) with those calculated from Equation 5.

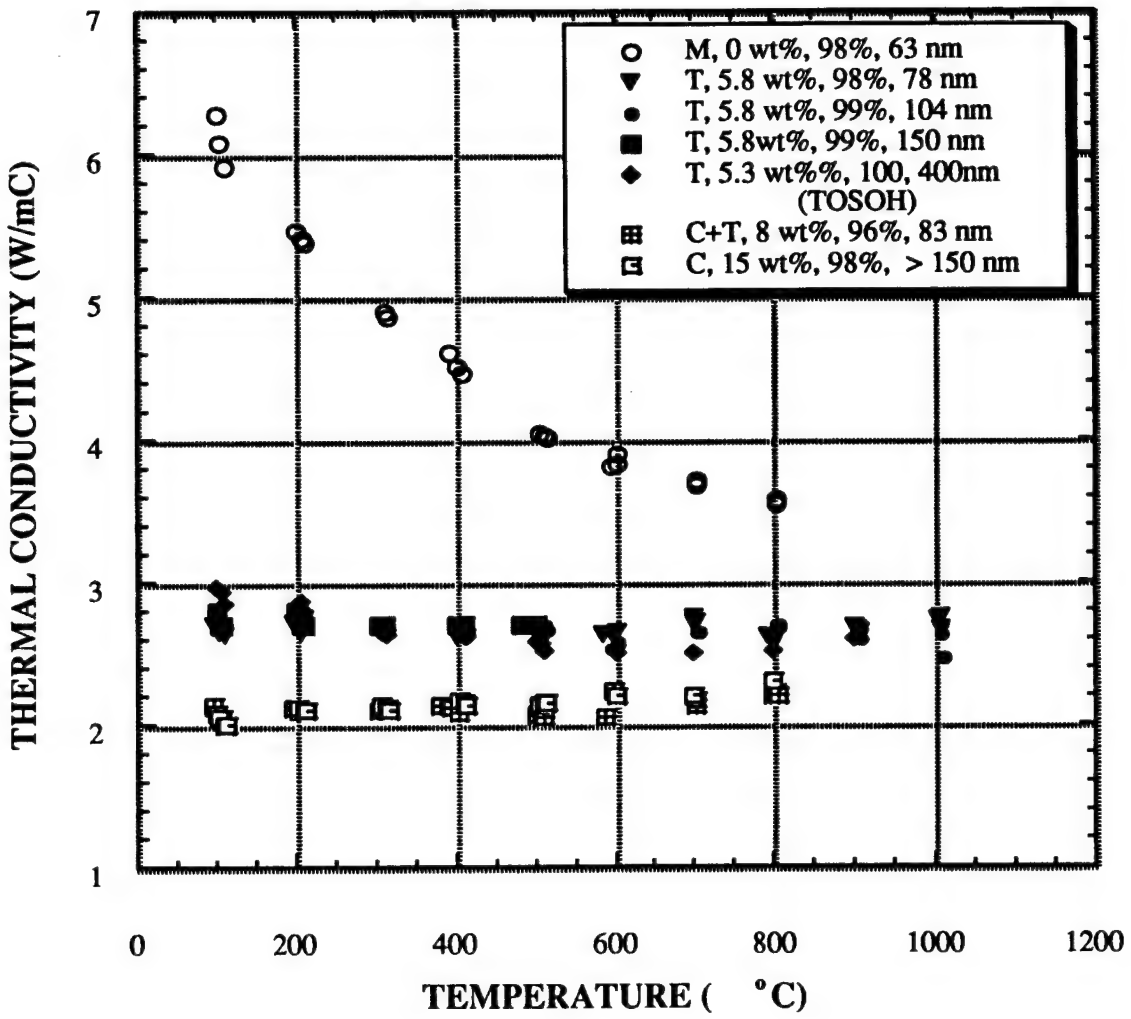

Figure 5.14. Effect of yttria content on thermal conductivity. Phases present in the samples are as follows: M=monoclinic, T=tetragonal, C=cubic. Densities (% of theoretical) and grain diameters (in nm) are also shown.

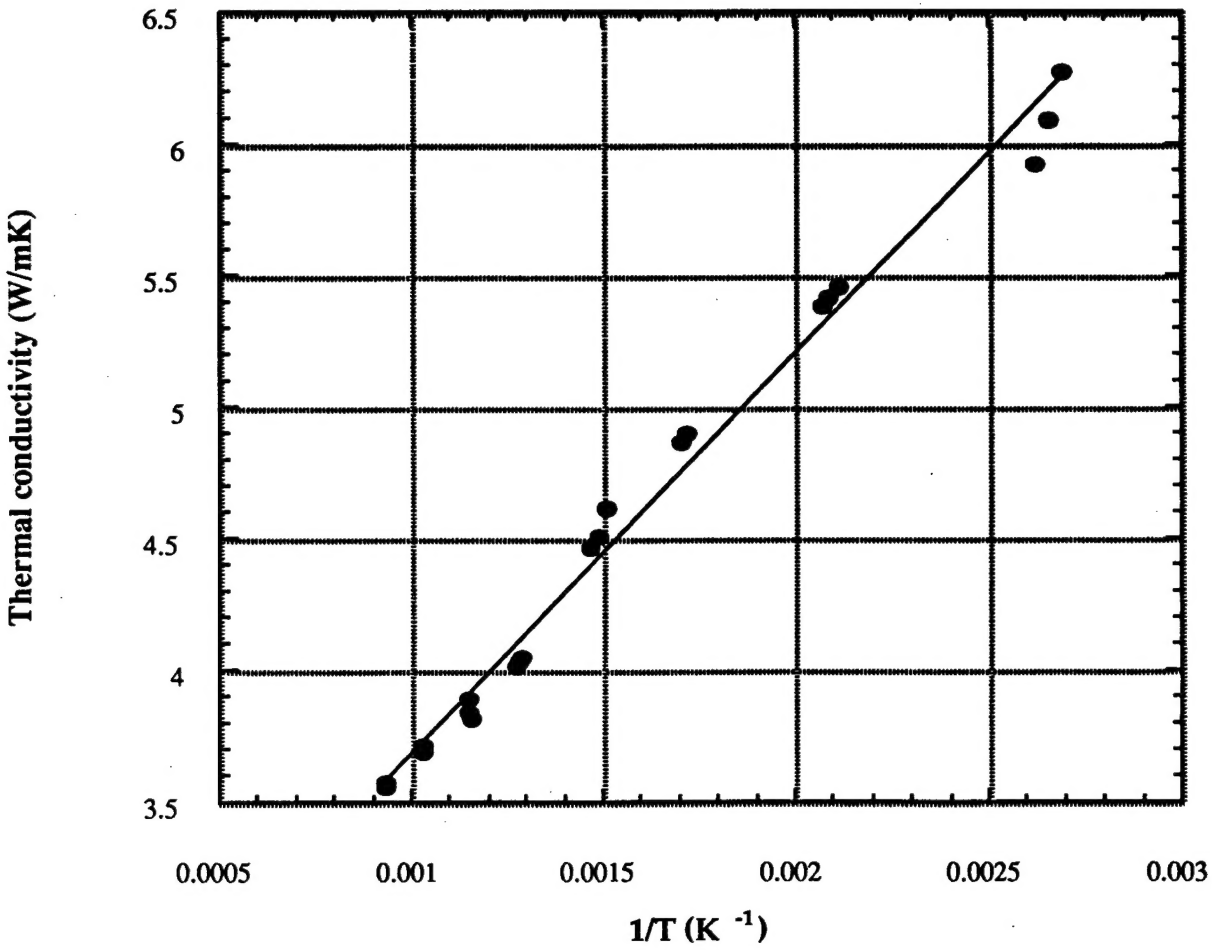

Figure 5.15. Thermal conductivity of pure monoclinic zirconia (98% dense, 63 nm grain diameter) vs 1/T

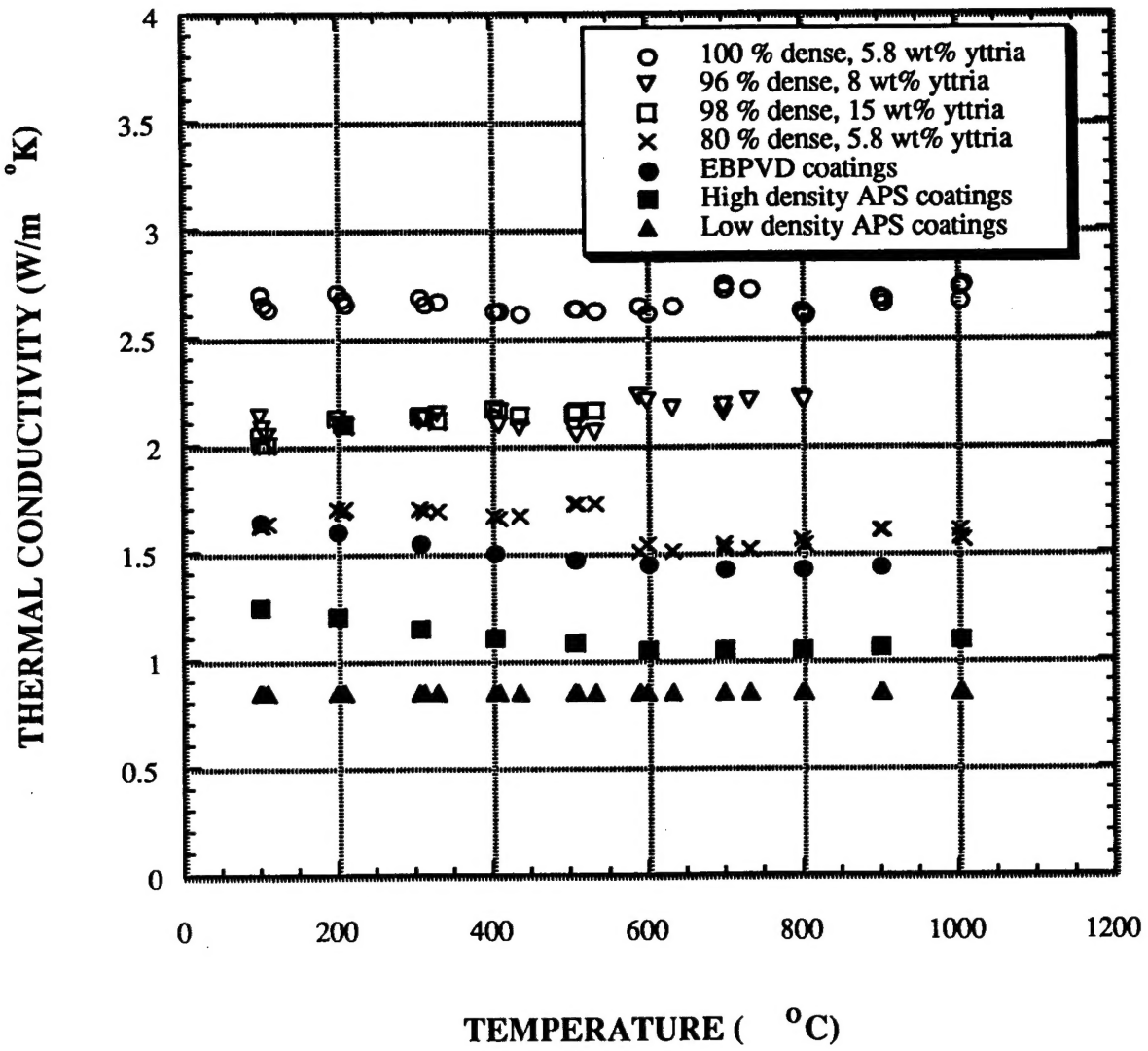

FIGURE 5.16. Comparison of thermal conductivity for nanocrystalline zirconias of the present study (open symbols) with comparable data for commercial zirconia thermal barrier coatings (closed symbols)

8.0 Collaborations, Presentations and Publications

Collaborations

As a result of the AFOSR Programs Workshop in Bar Harbor, ME in 1997, a collaboration between Dr. Jackson (GECRD) and Professor Reinhold Dauskardt, Department of Materials Science and Engineering, Stanford University, Stanford CA, was begun. This included supplying TBC coated samples to Dr.Dauskardt for his research on TBC failure stresses, and a visit by Dr.Dauskardt to GE-CRD.

As part of a Coolidge Fellowship Award from GECRD, Dr. Jackson spent a 3-month period visiting the Pennsylvania State University, working with Professor Jogender Singh of the Advanced Research Laboratory, using electron beam physical vapor deposition equipment to study FGM fabrication.

Dr. Srinivasan Raghavan and Professor Merrilea Mayo of the Department of Materials Science and Engineering, The Pennsylvania State University collaborated with Ralph Dinwiddie, Wally Porter, and Hsin Wang of the High Temperature Materials Laboratory, Oak Ridge National Laboratory, for measurements of the thermal properties of the nanoceramics, with Dr. Raghavan making several visits to Oak Ridge for experiments.

Publications and Presentations

M.J. Mayo, " Nanocrystalline Ceramics for Structural Applications: Processing and Properties," NATO-ASI on Nanostructured Materials: Science and Technology (St. Petersburg, Russia: Aug. 11 - 21, 1997). [presentation and publication]

Srinivasan Raghavan, Ralph Dinwiddie, Wally Porter, Hsin Wang and Merrilea Mayo, "The Effect Of Grain Size, Porosity And Yttria Content On The Thermal Conductivity Of Nanocrystalline Zirconia," paper to be published.

Srinivasan Raghavan, Ralph Dinwiddie, Wally Porter, Hsin Wang and Merrilea Mayo, "From nanocrystalline zirconia to thermal barrier coatings", A poster presented at the 1997 Cooperative Program in Metallurgy, The Pennsylvania State University

M.R. Jackson, A.M. Ritter, M.F. Gigliotti, A.C. Kaya and J.P. Gallo, "Multi-Phase Functionally Graded Materials for Thermal Barrier Systems," pp 33-38, Layered Materials for Structural Applications, MRS Symposium Proceedings Vol 434, J.J. Lewandowski, C.H. Ward, M.R. Jackson and W.H. Hunt, Jr., eds., MRS, Pittsburgh, PA [presentation at MRS April 9, 1996, and publication]

Presentations by M.R. Jackson were made at a number of laboratories during the period of the contract (travel and research time as part of the Coolidge Fellowship, the highest technical award granted by GECRD, for M. R. Jackson):

3/18/97, at The Pennsylvania State University, State College, PA: "Advanced High Temperature Materials - Composites and TBC Systems"
3/31/97, at Oak Ridge National Laboratories, Oak Ridge, TN: "Advanced High Temperature Materials - Composites and TBC Systems"
4/1/97, at The University of Tennessee, Knoxville, TN: "Advanced High Temperature Materials - Composites and TBC Systems"
4/3/97, at Johns Hopkins University, Baltimore, MD: "Advanced High Temperature Materials - Composites and TBC Systems"
4/15/97, at Adm Wayne Smith, Navy Repair Depots, Arlington, VA: "Advanced High Temperature Materials - Composites and TBC Systems"
4/15/97, at Hugh Montgomery, Director, Sci & Tech Req Div, Naval Operations-Crystal City: "Advanced High Temperature Materials - Composites and TBC Systems
4/8/98, at ONERA, Chatillon, FR: "Advanced Nb-based Silicide Composite Materials and TBC Systems"
4/15/98, at ONERA, Chatillon, FR: "FGM TBC Systems"
6/19/98, at Oxford University, Oxford, UK: "Advanced Nb-based Silicide Composite Materials and TBC Systems"
6/23/98, at Cambridge University, Cambridge, UK: "Advanced Nb-based Silicide Composite Materials and TBC Systems"